Experimental studies of three-photon ionization of Ba: Evidence of channel interference and Raman coupling

J. F. Kelly* and J. P. Hessler

Chemistry Division, Argonne National Laboratory, Argonne, Illinois 60439

G. Alber

Joint Institute for Laboratory Astrophysics, University of Colorado and National Bureau of Standards, P.O. Box 440, Boulder, Colorado 80309-0440

(Received 13 January 1986)

Three-photon ionization spectra of Ba were studied which result from two-photon resonances between the $6s^2\,{}^1S_0$ ground state and the $6snd\ J=2, 6s(n+1)s\ {}^1S_0$ $(16 \leq n < 40)$ Rydberg states and $5d7d\ {}^1D_2, {}^3P_{0,2}$ perturber states. A tunable laser with field strength $10^{-(4-5)}$ a.u. was used to drive the excitation in a low-density atomic beam $(n \lesssim 3 \times 10^8\ \mathrm{cm}^{-3})$. Resonant line shapes were systematically studied as a function of light polarization and intensity. Studies with linearly polarized light find all resonant line shapes manifest the same peak shift and asymmetry which is traced to the ac Stark shift of the ground state. The resonant peak height, shift, and linewidth scale linearly with light intensity which is accounted for with a rate-equation formulation. For the case of circular polarization, a distinct minimum of ionization occurs between each $J=2$ doublet of the $6snd$ series. One level (generally ${}^3D_2$) is significantly broadened in comparison to the laser linewidth $(0.1\ \mathrm{cm}^{-1})$ with increasing intensity while its sister level remains narrow $(\sim 0.2\ \mathrm{cm}^{-1})$. Further, light shifts of the ${}^3D_2$ states are generally $\geq 1\ \mathrm{cm}^{-1}$ to the red while shifts of ${}^1D_2$ states are negligible. This behavior switches for the $n=27$ doublet. Lastly, the dynamic shifts are not quadratic with the field strength. These effects are attributed in part to cancellation due to channel interference and a two-photon Raman process which mixes each $J=2$ doublet. These processes act in conjunction with the ac Stark effect to produce the observed profile behavior. The shifts and coupling of the excited states are attributed to the influence of the $6pnd\ J^\pi=3^-$ autoionization series and are shown to be sensitive to the singlet-triplet mixing coefficient β of the $J=2$ doublets. A perturbation analysis is introduced which accounts for the salient features of the data, although it does not include bandwidth and saturation effects. Calculations of light shifts of the $6snd\ J=2$ levels based on this analysis require β be modified from previous assignments based on hfs measurements for n in the vicinity of the $5d7d\ {}^1D_2$ perturber.

I. INTRODUCTION

Multiphoton ionization (MPI) which occurs near a discrete intermediate state will show effects of interference due to additional pathways to ionization.[1] Armstrong and co-workers have shown that any isolated resonant profile will manifest a Beutler-Fano—type profile due to interference with off-resonant pathways to ionization.[2] Their treatment describes the effect of interference in terms of a signed ratio of the transition matrix element for the resonant transition to that of the off-resonant processes.

Experimental observations of this intrinsic interference effect have been complicated by the fact that most MPI experiments done to date have been performed on low-lying levels of atomic systems. Interference effects are not expected to be very large since the atomic levels are widely separated in the experiments, so the off-resonant transition matrix element is very small.[3] The intrinsic effect is dominated generally by effects of light field-induced shifts and widths.

The rate of MPI through an isolated resonant level can be solved to good approximation with a rate-equation formulation if the rate of photoionization γ_r out of the resonant state dominates all other relaxation rates.[4] The MPI rate Γ is then given by

$$\Gamma = \frac{\Omega^2}{4} \frac{\gamma_r}{(\omega_{rg} - n\omega_L + S_{rg})^2 + \gamma_r^2}, \tag{1}$$

where Ω is the Rabi rate to populate the resonant state, ω_{rg} is the field-free separation of the initial and resonant levels, and S_{rg} is the net quadratic shift of these levels.[4] Most MPI experiments require a photon flux $F \geq 10^{25}$ (photons/cm^2 sec) to achieve measurable ionization signals which necessitate focusing a short-duration laser pulse in the sample to be ionized. Such experiments yield dispersion-shaped profiles for the ionization rate as a function of the laser detuning $\Delta = (\omega_{rg} - n\omega_L + S_{rg})$. The dispersive behavior is suggestive of an interference process but is primarily an artifact of averages of Eq. (1) over the spatiotemporal properties of the laser pulse.[3]

More pronounced effects of interference will occur when excitation is induced near two close-lying intermediate states such as a fine-structure doublet.[5-8] It was noted, however, that the lowest-order interference process is
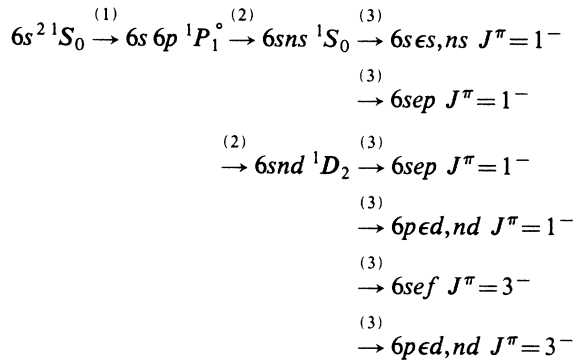
modified by a Raman-like scattering process r_{12} which couples the near-resonant states. The operator form of the process is[5]

$$r_{12} \propto \sum_j \frac{\langle 1 | \boldsymbol{\mu} \cdot \boldsymbol{\mathscr{E}} | j \rangle \langle j | \boldsymbol{\mu} \cdot \boldsymbol{\mathscr{E}} | 2 \rangle}{\omega_{j2} + \omega_L} . \qquad (2)$$

The coupling of the atom and light field is treated here with the dipole approximation where $\boldsymbol{\mathscr{E}}$ is the classical electric field associated with the light field and $\boldsymbol{\mu}$ is the dipole moment $e\mathbf{r}$ of the atom. Scattering between two near states $| 1 \rangle$ and $| 2 \rangle$ occur by virtual transitions to dipole-allowed intermediate states $| j \rangle$. Effects of the Raman coupling on the dynamics of photoionization,[6] the resonant MPI profiles,[7] and photoelectron angular distribution[8] have been studied theoretically. Recently, measurements of the photoelectron angular distribution produced by two-photon resonant, time-delayed third-photon ionization of Na $nd_{3/2,5/2}$ states have shown distinct effects of state mixing by this process.[9] This Raman process has also been invoked to explain nonquadratic light shifts of the $6d$ D_2 MPI resonances in Hg.[10]

In this work we present experimental measurements and theoretical analysis of MPI profiles which result from two-photon resonant, three-photon ionization of ground-state Ba atoms; a two-photon transition occurs between the $6s^2 \, {}^1S_0$ ground state and $6snd$ $J=2$ doublets ($n \sim 16$—40) followed by ionization. A single, quasimonochromatic laser was used to induce three-photon ionization and the integrated photoion signal was studied as a function of laser detuning.

Profound changes of the profiles occurred as the ellipticity of polarization was changed. Profiles obtained with circular polarization show evidence of channel interference and Raman coupling of the $J=2$ doublets. In the case of Ba, unlike the alkalis, the two-photon Raman coupling of Eq. (2) can consist of terms due to doubly excited autoionization states. For the case of circular polarization the magnitude of Eq. (2) is found to be comparable to the fine-structure splitting of the $6snd$ $J=2$ levels. Such a large coupling is a consequence of large ($6snd$ $J=2$)—($6pnd$ $J=3$) transition f values which are comparable to the ionic oscillator strengths of $\frac{1}{3}$ and $\frac{2}{3}$ for the $6s_{1/2}$-$6p_{1/2,3/2}$ transitions.[11] This can produce strong mixing of the doublet wave function and thus affect the position of the interference node. It also affects the positions of the resonances and leads to nonquadratic net shifts.[10]

For the case of circular polarization, we present a simple time-dependent perturbation model for the final-state probability amplitude. This model does not include bandwidth or saturation effects, yet it is found to reproduce the salient features of the channel interference and Raman coupling. Its simplicity allows easier interpretation of the behavior of the spectra.

Quantitative analysis of the spectra obtained with linearly polarized light is less complete because of the complication of including $J^\pi = 1^-$ final states. It is noted that the spectra can be treated to good accuracy as an incoherent superposition of isolated resonances, so a rate-

FIG. 1. Ba I energy-level diagram. The excitation scheme for three-photon ionization is shown occurring via two-photon resonances with even-parity $J=0$ and $J=2$ intermediate states. The excitation pathways for linearly polarized light are depicted with dashed arrows and that for circularly polarized light is shown as a solid arrow. The latter excitation is redepicted to show the Raman scattering process due to $6pnd$ autoionization levels.

equation description [Eq. (1)] is used to analyze these data.

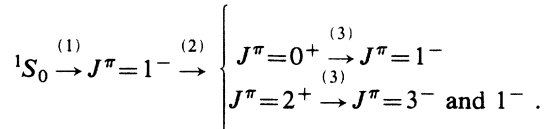## II. EXPERIMENTAL DETAILS

A. Excitation scheme

Figure 1 depicts schematically the three-photon ionization scheme used in this experiment. Several intermediate $J^{\pi}=2^{+}$ states are noted for later reference.[12] The assignment of singlet or triplet character is very arbitrary for the $6snd$ levels near the $5d\,7d\,^{1}D_{2}$ perturbing level; the assignments in this work follow those of Ref. 12 for convenience only. A single laser source induced two-photon resonant, three-photon ionization of the $^{1}S_{0}$ ground state. The excitation channels are depicted for purely linear and circular polarization.

For the case of linearly polarized light, the selection rules are $\Delta J=1$ and $\Delta m_{J}=0$ for each step in the multiphoton process. If configuration interaction (CI) and spin-orbit interaction were negligible, the three-photon transitions would proceed from the $^{1}S_{0}$ ground state via the intermediate pathways

$$6s^{2}\,^{1}S_{0} \xrightarrow{(1)} 6s\,6p\,^{1}P_{1}^{\circ} \xrightarrow{(2)} 6sns\,^{1}S_{0} \xrightarrow{(3)} 6s\epsilon s, ns \quad J^{\pi}=1^{-}$$

$$\xrightarrow{(3)} 6sep \quad J^{\pi}=1^{-}$$

$$\xrightarrow{(2)} 6snd\,^{1}D_{2} \xrightarrow{(3)} 6sep \quad J^{\pi}=1^{-}$$

$$\xrightarrow{(3)} 6p\epsilon d, nd \quad J^{\pi}=1^{-}$$

$$\xrightarrow{(3)} 6sef \quad J^{\pi}=3^{-}$$

$$\xrightarrow{(3)} 6p\epsilon d, nd \quad J^{\pi}=3^{-}$$

Since CI and spin-orbit effects are large in barium, additional intermediate levels will contribute to the transition amplitudes. The $^{1}S_{0}$ ground state is a mixture of $6s^{2}$, $5d^{2}$, and $6p^{2}$ configurations, so apparent two-electron jumps are allowed. For example, the transitions $6s^{2}\,^{1}S_{0}-5d\,6p\,^{3}D_{1}^{\circ}$ and $^{3}P_{1}^{\circ}$ occur with oscillator strengths f_{ik} of order ~ 0.01 for each transition.[13] In general, the three-photon transitions will proceed via all bound and continuum intermediate states such that

$$^{1}S_{0} \xrightarrow{(1)} J^{\pi}=1^{-} \xrightarrow{(2)} \begin{cases} J^{\pi}=0^{+} \xrightarrow{(3)} J^{\pi}=1^{-} \\ J^{\pi}=2^{+} \xrightarrow{(3)} J^{\pi}=3^{-} \text{ and } 1^{-} . \end{cases}$$

For the case of circularly polarized light, the selection rules require $\Delta J=1$ and $\Delta m_{J}=\pm 1$ where the plus (minus) sign applies for right- (left-) handed ellipticity. Three-photon ionization will proceed via all intermediate states such that

$$^{1}S_{0} \xrightarrow{(1)} J^{\pi}=1^{-} \xrightarrow{(2)} J^{\pi}=2^{+} \xrightarrow{(3)} J^{\pi}=3^{-} .$$
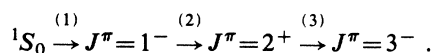
B. Experimental apparatus

The experimental setup is depicted schematically in Fig. 2. Three-photon ionization spectra were produced by focusing the output of a tunable dye laser (~ 1 mJ/pulse) into an effusive beam and collecting the charged photofragments with a parallel-plate capacitor. A low-density atomic beam ($n \sim 10^{8}$ atoms/cm^{3}) was used as the sample to avoid spurious space-charge effects. The charged products were collected by application of a dc or pulsed bias voltage and the resultant currents were integrated and shaped using standard low-noise charge-to-voltage (CV) preamplifiers and amplifiers (Ortec 142IH preamplifiers and 572 amplifiers). The detector and lead capacitance was such that the rms noise of the preamplifier and amplifier amounted to ≤ 560 electrons per laser pulse. A channel electron multiplier (CEM; Galileo) was later used to measure the photoelectron flux emitted, under field-free conditions, into an perture in the deflection plate (5×10^{-4} sr). The CEM was biased at gains $\sim 10^{4}$ which provided a relative analog signal with comparable S/N ratio to the capacitor detector.

Provision was made to measure the absolute laser pulse energy with a thermopile (Scientech series 360) before and after each wavelength scan. The thermopile was posi-
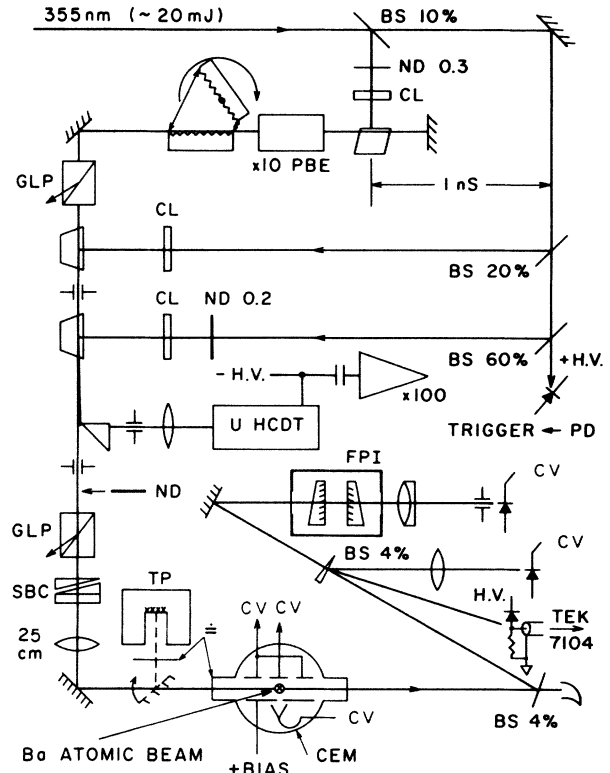
FIG. 2. Schematic of the experiment. Optical components: BS, beam splitter; FPI, Fabry-Perot interferometer; GLP, Glan laser prism; ND, neutral-density filter; PBE, prism beam expander; SBC, Soleil-Babinet compensator. Electronic components: CEM, channel electron multiplier; CV, charge-to-voltage preamplifier; PD, p-i-n photodiode; TP, thermopile. The dye laser [C-480$\sim$(1×10^{-2})M] was pumped by the third harmonic of a Nd:YAG (yttrium aluminum garnet) laser (Quanta Ray DCR-2 at 10 pps).

tioned immediately after the Soleil-Babinet compensator (SBC) and lens. Care was taken to compensate for losses of the cell entrance window and beam steering mirror so that absolute errors of the pulse energies are $\leq 5\%$. During a scan, measurements of the relative laser pulse energy were made with a calibrated photodiode and CV preamplifier. Temporal characteristics of the pulses were monitored with a fast photodiode assembly (HP-4220 with rise and fall times $\tau_r,\tau_f \sim 120$ psec) coupled to a 1-GHz oscilloscope (TEK 7104).

Wavelength calibrations were obtained by concurrently monitoring the optogalvanic signal from a uranium hollow cathode discharge tube (HCDT) and the transmission signal of a temperature-stabilized Fabry-Perot étalon.

Data acquisition was performed with an LSI 11/23 minicomputer equipped with a 16-bit, multichannel analog-to-digital converter (ADC). The pulsed signals were time averaged with boxcar integrators (PAR 162/164 and Evans Associates 4130) and their outputs were sampled by the ADC.

For completeness, a detailed discussion of noteworthy characteristics, procedures, or problems with the apparatus is given below.

1. Dye laser

Light pulses with a time-averaged bandwidth $\bar{b} \approx 0.10$ cm^{-1} [full width at half maximum (FWHM)] were generated with a Littman double-grating oscillator[14] and amplified through two stages of transversely pumped dye cells. The bandwidth of the laser was studied with a moderate-finesse ($F \approx 80$) Fabry-Perot interferometer and actually consisted of $\sim 3-4$ frequency modes per pulse; each mode, designated by i, had a bandwidth $b_i \lesssim 0.01$ cm^{-1} and the modes were equally spaced ≈ 0.02 cm^{-1} apart. (This spacing corresponds to the longitudinal free spectral range of the oscillator cavity.) The central mode was dominant in general, but its frequency fluctuated on a shot-to-shot basis to give $\bar{b} \approx 0.10$ cm^{-1}. Figure 3(a) shows a time-averaged spectrum of the dye laser. The temporal structure of the dye-laser pulses was quite complex at the 1-ns time scale as shown in Fig. 3(b). The resolved temporal fluctuations manifested a ~ 600-MHz beat frequency which is consistent with the mode spacing noted previously.

The output of the dye laser was filtered with air-spaced Glan polarizing prisms (Karl Lambrecht). The laser light produced by the dye-laser oscillator was linearly polarized to a high degree ($s:p \leq 10^{-2}$) so the Glan prisms acted primarily as partial filters of the randomly polarized spontaneous dye fluorescence ($< 12.5\%$ of the total pulse energy after the second Glan prism and iris). The ellipticity of the filtered light was changed using a Soleil-Babinet compensator (Karl Lambrecht BSA-13-6). The compensator spacing was adjusted for $\lambda/4$ wave retardation, for a given wavelength range, by tuning the laser to a two-photon resonant transition with a $J^{\pi}=0^+$ state and nulling the ionization signal with the fast axis of the compensator set at $\pm 45°$ to the incident plane of linear polarization. Linear polarization was maintained with the fast axis set parallel (orthogonal) to the incident plane of po-

larization, while intermediate degrees of elliptical polarization were obtained between these positions.

2. Light flux measurements

The average laser intensity I impinging on the atomic beam was calculated from measurements of the beam profile and divergence. The spatial profile of the dye laser was first measured photometrically by mechanically scanning a single element photodiode across an expanded image of the beam. The profile was elliptical with a major to minor axis ratio of 1.3:1. During the course of experiments, the profile was monitored by measuring burn patterns. A full angle beam divergence of ≈ 0.56 mrad $\pm 35\%$ was calculated from measurements of the beam spread. A 25-cm focal length, double-convex spherical lens focused the dye-laser pulse to a calculated beam diameter of 140 μm ($\pm 35\%$) at the focal point. A 0.5-mJ pulse is calculated to produce $I_0 \approx 1.1$ GW/cm^2 at the focal center. The intensity of the laser was varied by adding neutral density (ND) filters before the second Glan polarizing prism. The addition of the ND filters did not affect the burn-pattern profiles to any visually evident extent.
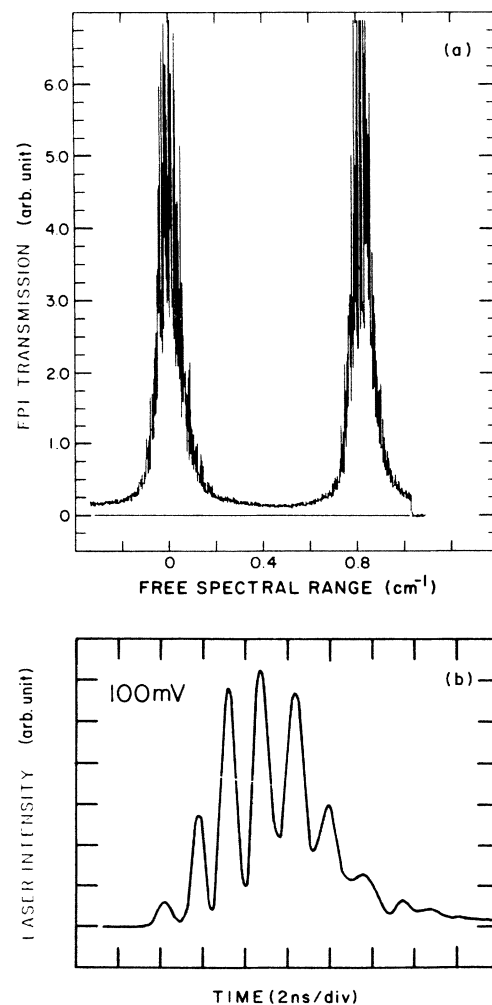

FIG. 3. Dye-laser characteristics: (a) time-averaged spectrum of the dye laser, (b) dye-laser temporal behavior. The results are typical for the scans given in this work.

This same dye laser and optical train would produce second-harmonic generation (SHG) with a conversion efficiency of $\approx 1.1\%$ in a C-cut KPB crystal (Inrad) when $\lambda_0 \approx 4860$ Å and $I_0 \approx 2$ GW/cm^2. Measurements of SHG may provide a reliable means to monitor spatial profile variations, but was unavailable for use during this work.

3. Frequency calibration

The absolute energy scales for the MPI spectra were obtained from a least-squares fit of the optogalvanic effect (OGE) spectra to a quadratic function of the wavenumber values of an emission line atlas.[15] The emission line positions were obtained with a different HCDT (Westinghouse, WL-36077) than that used in this work (Instrumentation Laboratory, No. 62826); however, independent calibrations indicate any instrumental offsets are < 0.005 cm^{-1}.[16] The error in the absolute wavenumber calibration of $2\bar{\nu}_L$ was typically ≤ 0.07 cm^{-1} when there were four or more unblended uranium lines uniformly spanning an MPI spectrum. Additional frequency marks were provided by monitoring the transmission of a temperature-stabilized interferometer (drift < 0.05 cm^{-1}/hr). Relative variations of spectral features could thus be calibrated to ≤ 0.05 cm^{-1} for most sets of scans.

4. Atomic beam

A thermal beam of Ba atoms was produced with a resistively heated crucible and collimation orifices. Angu-

lar spread of the beam was kept < 0.1 rad so that residual Doppler broadening of the spectra was ≤ 0.06 cm^{-1}. Coaxial, bifilar heating wire (Amperex, Thermocoax INCI15) was used with the electric current constrained to return along the sheath to help minimize stray magnetic fields. The temperature of the oven was monitored with a thermocouple press fitted into a recess in the crucible as close to the sample as possible.

The crucible assembly was operated typically at (660 ± 2)°C for all spectra presented in this work. Calculations of the effusive parameters were based on number density measurements inside the crucible which were based on the barium vapor density equation.[17] The profile of the beam was established from thin film interference patterns that developed on a quartz window positioned directly above the beam/detector assembly. The noted operating temperature resulted in a maximum number density $n_{max}(r=0) \approx 2.9 \times 10^8$ (atoms/cm^3) at the focal center. The atomic beam density fell off radially as $1 - r/r_0$ where $r_0 = 0.32$ cm was the calculated cutoff radius of the beam at the focal position.

The single most important consideration for obtaining high-quality two-photon resonant, three-photon ionization of barium is the surface preparation of the even assembly. It was discovered, accidently, that the oven assembly must have an extremely durable and complete oxide coating in order to obtain clean MPI spectra. It is speculated that the oxide coating inhibits the rate of thermionic emission by the oven assembly.

The initial sets of MPI measurements were performed with unoxidized stainless-steel oven assemblies that were
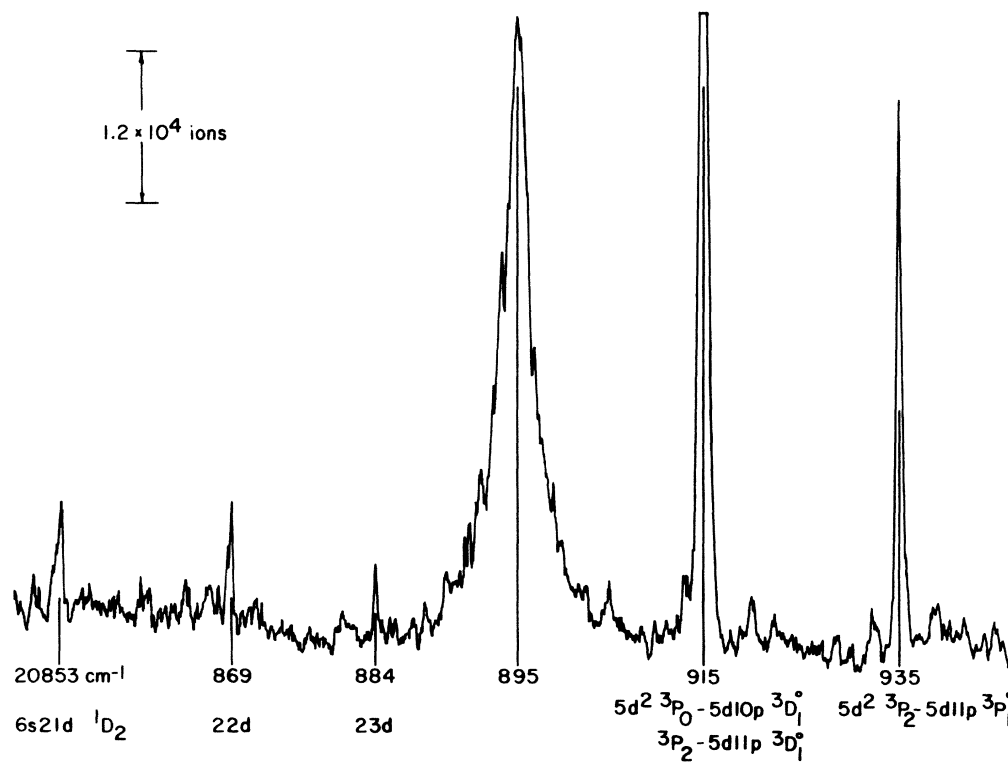
FIG. 4. Anomalous resonances due to excited Ba atoms. Shown is an MPI spectrum obtained with an unoxidized stainless-steel oven and $I_0 \sim 0.5$ GW/cm^2. The baseline is shown for the case of no light.

thoroughly cleaned and outgassed at elevated temperatures ($T \geq 900\,°C$, $P < 5 \times 10^{-7}$ Torr) before being loaded with a charge of barium. The MPI spectrum obtained with these assemblies consisted of a series of photoionization resonances from excited states of Ba and a substantial background ionization signal superimposed with a weak MPI spectrum. Figure 4 shows an example of such a spectrum.

Many of the resonances were identified with one-photon transitions from ^3P_j states of the $5d^2$ configuration to $5dnp$ and $5dnf$ autoionization states above the $6s$ ionization limit.[18] Several of these resonances were reexamined at higher resolution and were found to manifest Beulter-Fano profiles that were asymmetrically broadened to higher frequencies like those reported for the $6s^2\,{}^1S_0-5dnp\,{}^3P_1{}^\circ$ photoabsorption spectra.[18]

A possible mechanism for excitation of the $5d^2$ states is recombination from Ba^+ ions produced by electron impact with thermionic electrons. It was noted that MPI spectra obtained without a bias field exhibited no evidence of these resonances, whereas all MPI spectra obtained with bias fields (a > 10-V potential difference existed between the bias field plate and crucible in this work) showed some evidence of anomalous resonances and greater shot noise.

III. RESULTS

Examples of the MPI spectra are shown in Figs. 5(a) and 5(b), respectively, for the cases of linearly and circularly polarized light fields. The MPI signal was measured as a function of the laser frequency for fixed light intensity. The data shown in Figs. 5 were obtained with the capacitor detector using a dc bias field of 8 V/cm. Figures 6(a) and 6(b) show a closeup of the spectrum near the $5d\,7d$ perturber. These spectra were obtained under nearly bias-free conditions (< 0.2 V/cm) using the CEM detector.[19]

The disappearance of MPI resonances corresponding to $J=0$ intermediate states, for the case of circularly polarized light, is an obvious consequence of the angular momentum selection rules. What is very striking, however, is the variation of the resonance line shapes with changing ellipticity of light polarization. For the case of linearly polarized light, all resonant MPI spectra were asymmetrically broadened toward longer, red wavelengths. The magnitude of the linewidths (FWHM) and asymmetry were independent of the n or l quantum numbers probed in this study. Using circularly polarized light, the resonances associated with the $6snd\,{}^1D_2$ states significantly narrowed by a factor of 2 and manifested an asymmetry toward shorter, blue wavelengths. By contrast, resonances associated with the $6snd\,{}^3D_2$ states noticeably broadened by a factor of 3 further to the red.

Figure 7 shows the progressive alteration of the resonant MPI line shapes with changes of the ellipticity of light polarization. A noticeable minimum of ionization between the $J=2$ doublets develops for the case of circularly polarized light. These data were obtained with the parallel-plate capacitor. An additional resonance feature was partially resolved in the spectra and its wave-number
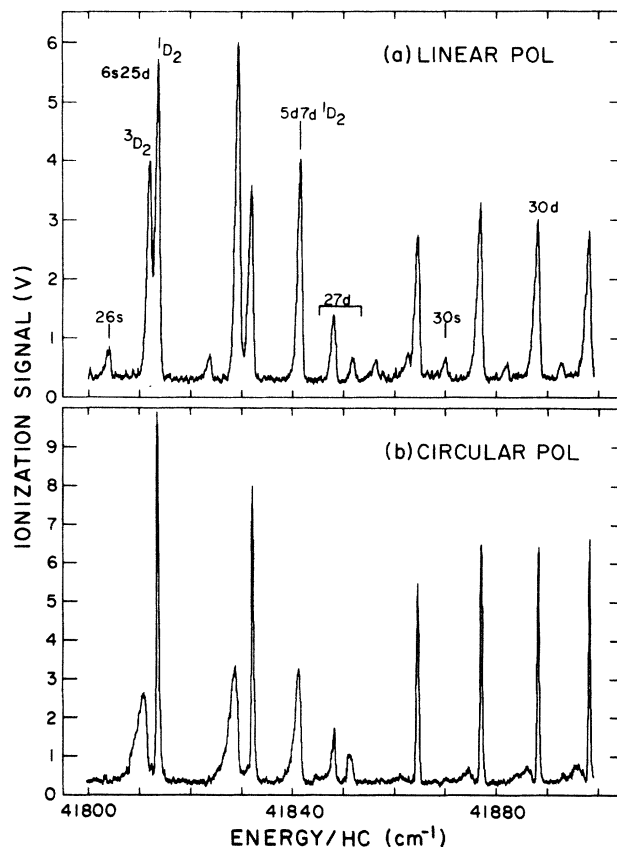
FIG. 5. MPI spectra: (a) linear polarization, (b) circular polarization. An 8-V/cm dc bias was used to collect the ions and $I_0 \approx 1.5$ GW/cm^2 at the focal center. A 1-V signal amplitude corresponds to 8.0×10^3 ions ($\pm 10\%$).
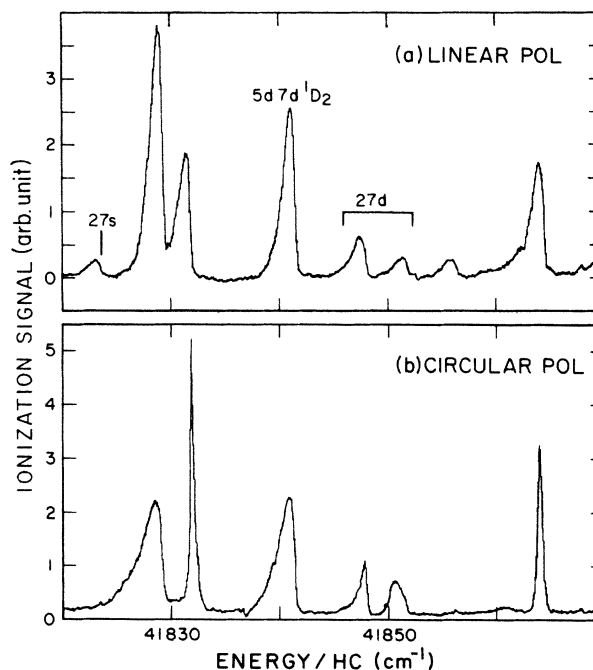

FIG. 6. MPI spectra: (a) linear polarization, (b) circular polarization. These data were obtained with the CEM detector without a bias field and $I_0 \approx 1.1$ GW/cm^2.
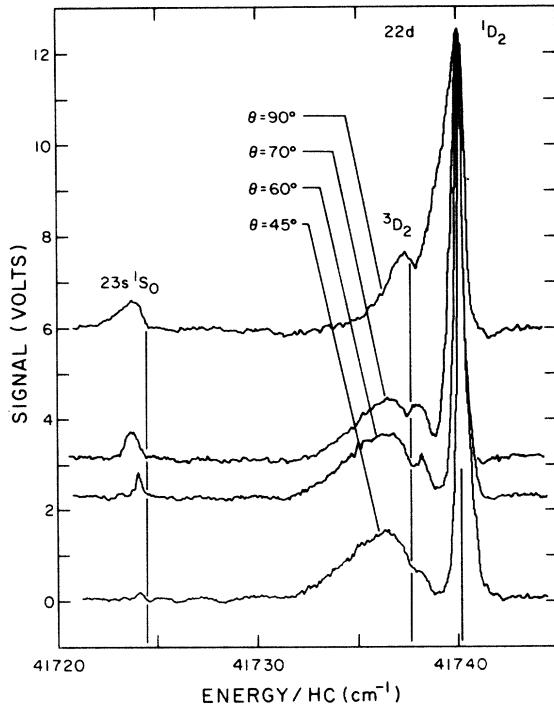
FIG. 7. MPI spectra vs polarization. Note that the baselines have been deliberately offset. Hatched lines identify the positions of the $6s\,23s\,^1S_0$ and $6s\,22d\,^{3,1}D_2$ levels (Ref. 12). The angle θ is the angular separation of the fast axis of the compensator measured with respect to the initial plane of polarization of the laser. l denotes linear, c denotes circular; then $I_l \propto [\cos(2\theta)]^2$ and $I_c \propto [\sin(2\theta)]^2$. (The dc bias is 4 V/cm, $I_0 \approx 1.4$ GW/cm^2, and 1 V$\rightarrow$9.1$\times$10^3 ions.)

position was identified with the $6s\,23pP^\circ$ level value.[20] The appearance of the $6snp\ J^\pi = 1^-$ spectra is attributed to Stark mixing of the even- and odd-parity series by the static bias field.[21] Stark effects are acute in Ba since the $6s(n+1)p$ (Ref. 20) and $6s\,24f$ (Ref. 22) levels are nearly degenerate, respectively, with the $6snd$ and $5d\,7d\,^1D_2$ levels. The MPI resonance features were systematically restudied as a function of the static bias field to confirm this. The peak heights of the Stark mixed features were observed to scale quadratically with the bias field for low field strengths (<100 V/cm at $n=22$) and π orientation of the light field and bias field axis.

A. Intensity dependence of resonant MPI spectra

The MPI spectra which result from resonances with the $6s\,22d\,^{3,1}D_2$ and $6s\,23s\,^1S_0$ states were studied systematically with light intensity. These resonances were chosen for study because six strong uranium OGE transitions bracket the spectrum. The relative calibration errors for the two-photon energies of these spectra, in units of wave numbers, are <0.03 cm^{-1}.

1. Linear polarization

The variation of the resonant MPI spectra with light intensity is shown in Fig. 8. The peak position of the resonance due to the $6s\,22d\,^1D_2$ state shifted linearly with intensity ≈ 0.35 cm^{-1} to the red when the laser pulse energy was increased from 0.105 to 1.05 mJ/pulse. A notable feature of these MPI spectra is the sharp onset of resonance which occurs very near the published wave-number values for the $(6s^2\,^1S_0)-(6snl\ \ J=0,2)$ transition energies.[12] The published data were obtained under conditions of much lower light intensity than the data presented here (<1 MW/cm^2 versus ~ 1 GW/cm^2). The peak positions of this work were all systematically red shifted from the earlier data by ~ 0.5 cm^{-1} when $I_0 \sim 1.1$ GW/cm^2 at the focal center of the pulse.

The intensity dependence of the $6s\,23s\,^1S_0$ and $6s\,22d\,^1D_2$ MPI resonance linewidths γ (FWHM) is shown in Fig. 9(a). These linewidths varied linearly with intensity for the entire range of incident intensities. The extrapolated zero-intensity linewidths γ_0 were twice the time-averaged laser linewidth $\bar{b}$. The intensity dependence of the $^1D_2$ peak height is shown in Fig. 9(b). The peak height was measured after subtracting an off-resonant ionization signal which varied linearly with light intensity and not as I^3. (The baseline ionization signal may be due to a direct photoionization process of diffusion oil products.) The $^1D_2$ feature shows some evidence of saturation at the highest intensities. The quadratic intensity dependence of the integrated ion yield is shown in Fig. 10. The total area under the $J=2$ doublet
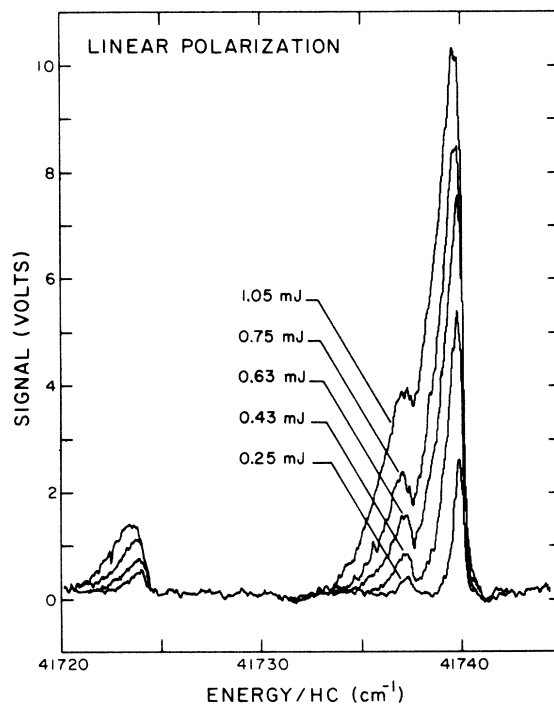

FIG. 8. MPI spectra ($6s\,22d\ J=2$ and $6s\,23s\,^1S_0$) vs light intensity; linear polarization. A pulse energy of 1 mJ$\rightarrow I_0 \approx 2.2$ GW/cm^2, bias equals 4 V/cm, and 1 V$\rightarrow$9.1$\times$10^3 ions.
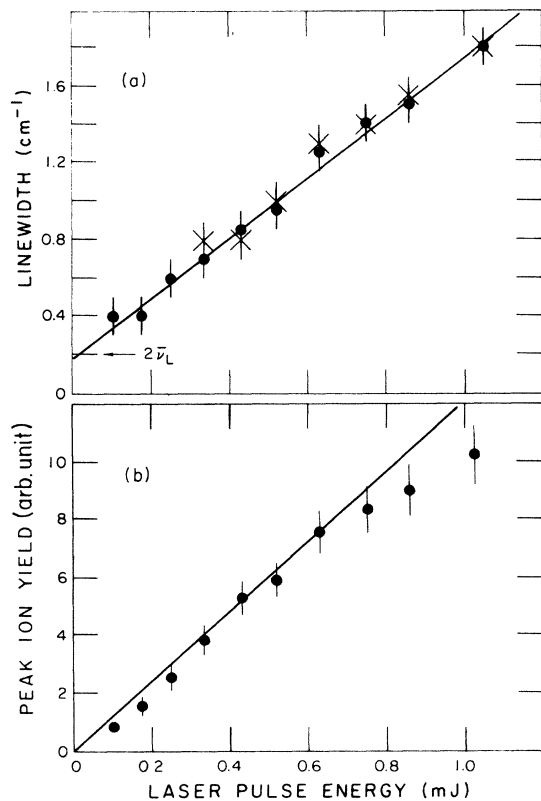
FIG. 9. (a) Intensity dependence of the MPI linewidths (FWHM): $\times$, $6s\,23s\ {}^1S_0$; $\bullet$, $6s\,22\ {}^1D_2$. (b) Intensity dependence of the $6s\,22d\ {}^1D_2$ peak height.

2. Circular polarization

The intensity behavior of these same spectra, using circularly polarized light, is shown in Fig. 11. The resonance associated with the ${}^1D_2$ state broadens asymmetrically to the blue with increasing intensity but its peak position and the minimum remain nearly fixed within the experimental limits of calibration. In contrast, the resonance associated with the ${}^3D_2$ state noticeably broadens and shifts to the red.

The intensity dependence of the $6s\,22d\ {}^1D_2$ resonance linewidth γ (FWHM) and peak height are shown in Fig. 12. At low intensities, the peak height scaled nonlinearly ($\approx I^{1.6}$) with light intensity, whereas the integrated ion yield for the ${}^1D_2$ resonance scaled quadratically with intensity. This implies the linewidth should scale slower than linear, which was the case at low intensities ($\sim I^{0.4}$). Figure 13 shows the intensity dependence of the integrated ion yields. Results are shown for each resonance since they can be resolved clearly. Again, the ${}^1D_2$ resonance shows evidence of saturation at light intensities where the peak and total ion yields are comparable to the total ground-state population in the focal volume.

B. Relative measurements of the photoion yield

Measurements of the MPI spectra were obtained with the CEM detector for light intensities sufficient to detect the weaker $6sns\ {}^1S_0$ features, but not strong enough to cause evident saturation effects of the stronger $6snd$ features. The integrated MPI signals are given in Tables I–III; the data are normalized to the integrated signal for the $6s\,22d\ {}^1D_2$ resonance obtained with linear polarization

was plotted since the individual resonances were not entirely resolved at the highest intensities. Evidence of saturation is also apparent at the highest light intensities used. It is attributed to ground-state depletion of Ba atoms in the focal volume, because the rolloff occurs when the total photoion yield $\sim n_{max} \times$(focal volume).

FIG. 10. Intensity dependence of (integrated ion yield $6s\,22d$ doublet)$^{1/2}$.
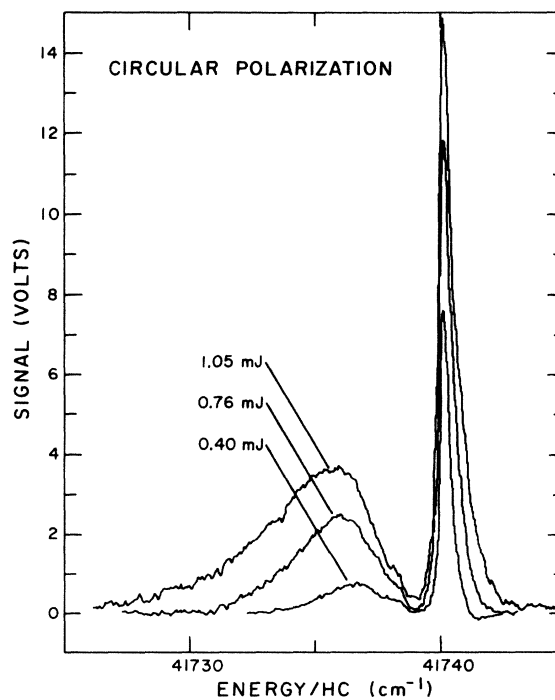

FIG. 11. MPI spectra ($6s\,22d\ J=2$) vs light intensity; circular polarization. Other parameters identical to Fig. 8.
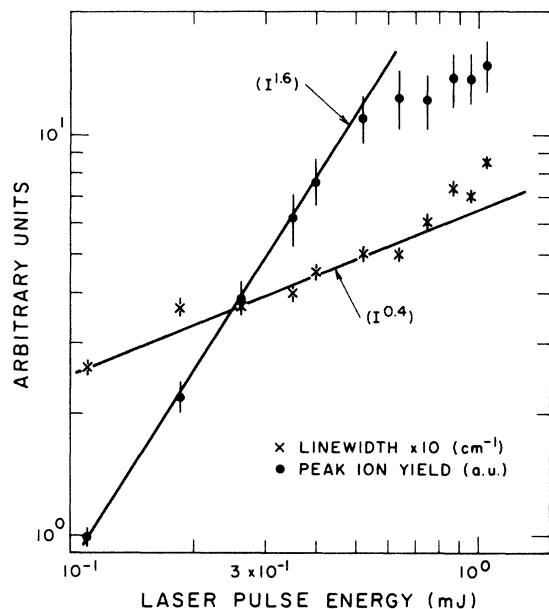
FIG. 12. Intensity dependence of the $6s\,22d\ ^1D_2$ resonance linewidth (FWHM) and peak height for the case of circular polarization.

and $I_0 \sim 1.1$ GW/cm^2. Also listed are the peak positions of the resonances.

Sources of error for the ion yield stem principally from two instrumental effects when the resonances can be clearly resolved.

(1) A nonlinearity of the CEM detection efficiency, perhaps due to space-charge effects at the aperture, leads to a reduction of the peak signal strength for the stronger resonances studied. The linearity of this detector was calibrated against results from the parallel-plate capacitor. The linearity of the latter should be better than 0.2% (the preamplifier and amplifier linearity) in the absence of background scattering since its dimensions are substantially larger than any drift dimensions of the ions. The noted error resulted in $\leq 5\%$ reductions for the strongest resonances when $n \geq 21$ and $> 5\%$ errors when $n < 21$. Stark mixing effects preclude using the parallel-plate detector for measurements of photoion yield when $n \geq 25$.

(2) Signal-averaging procedures and finite sampling rates tended to reduce the integrated signal. This effect is line-shape dependent and was experimentally assessed by rescanning selected features at "quasistatic" rates. Processing errors are $\approx 5\%$ for the case of linear polarization. They are $< 5\%$ for the broad features and $\sim 10\%$ for the narrowest features in the case of circular polarization. Thus for well-resolved resonance profiles, the relative errors are generally $\sim 10-15\%$ for $6sns\ ^1S_0$; $\sim 10-15\%$ for resolved $^3D_2$ states, $n < 27$; 15–20% for $^1D_2$, $n < 30$ (linear polarization), and 15–25% (circular polarization). Larger relative errors occur when the resonances are blended with neighboring features.

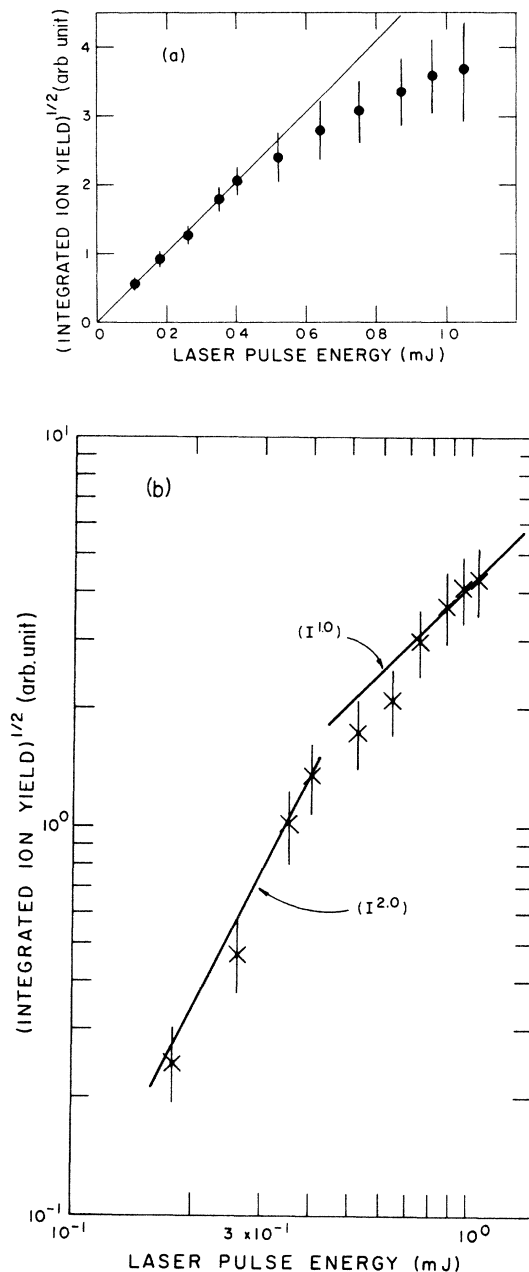FIG. 13. (a) Intensity dependence of (integrated ion yield)$^{1/2}$: ●, $6s\,22d\ ^1D_2$. (b) Intensity dependence of (integrated ion yield)$^{1/2}$: ×, $6s\,22d\ ^3D_2$.

IV. THEORY

An analysis of the MPI resonance profiles which includes bandwidth and saturation effects will not be attempted in this work since the present simplified analysis gives a clear indication of the physics involved. Profile calculations will be made assuming a square pulse output of monochromatic light for the laser. A time-dependent perturbation analysis is used to calculate the probability

TABLE I. Peak positions and integrated ion yield for two-photon resonant, three-photon ionization of $\Delta J = 0$ intermediate levels; linear polarization, $I_0 \approx 1.1$ GW/cm^2.

Designation	Peak position, $2\bar{\nu}_L$ (± 0.15 cm^{-1})	Integrated MPI rate[a] (rel. units)
$5d\,7d\,^3P_0$	b	1.22
$6s\,18s\,^1S_0$	b	0.28
$6s\,19s\,^1S_0$	41 534.9	0.12
$6s\,20s\,^1S_0$	41 595.4	0.11
$6s\,21s\,^1S_0$	41 645.65	0.12
$6s\,22s\,^1S_0$	41 688.5	0.115
$6s\,23s\,^1S_0$	41 723.75	0.08
$6s\,24s\,^1S_0$	41 754.75	0.06
$6s\,25s\,^1S_0$	41 780.7	0.05
$6s\,26s\,^1S_0$	41 803.4	0.04
$6s\,27s\,^1S_0$	41 823.1	0.05
$6s\,29s\,^1S_0$	41 855.9	0.05
$6s\,30s\,^1S_0$	41 869.55	0.03
$6s\,31s\,^1S_0$	41 881.5	0.03

[a]Normalized with respect to the integrated ionization rate for the $6s\,22\,^1D_2$ resonance (linear polarization).

[b]OEG spectra were not available for calibration.

amplitudes a_g, a_1, and a_2 for the ground state and two near-resonant intermediate states. In this analysis, state $|1\rangle$ refers to the lower-energy level of the $J=2$ doublets. The transition probability for ionization is obtained in terms of these amplitudes as[5]

$$P_{\text{ion}} = 1 - (\,|a_g|^2 + |a_1|^2 + |a_2|^2\,) .$$
(3)

It is assumed that losses from these states to other states by collisions or radiative transitions are negligible in comparison to the photoionization rate. For comparison, the radiative rates out of the $6snd$ $J=2$ states are $< 5 \times 10^6$ sec^{-1} for $n \geq 16$. In contrast, it will be shown presently that photoionization rates out of these states are $\gtrsim 10^9$ sec^{-1} when $I \approx 1$ GW/cm^2.

The Hamiltonian for the system is taken to be

$$H = H_A - \boldsymbol{\mu} \cdot \mathbf{E}(t) ,$$
(4)

where the coupling of the field and atom is approximated by the electric dipole interaction. Here H_A is the field-free atomic Hamiltonian, $\boldsymbol{\mu}$ is the atomic electric dipole operator, and the electric field operator $E(t)$ is given as

$$E(t) = \mathscr{E}_0 e^{-i\omega_L t} + \text{c.c.}$$
(5)

[The value of the electric field (in MKS units) is given by $I = (c\epsilon_0/2)E^2$. An intensity $I = 1$ GW/cm^2 converts to an electric field $E \approx 0.85 \times 10^{-4}$ a.u. in the rest frame of the atom.]

The time-dependent Schrödinger equation is solved in the usual way by expanding the wave function as

$$|\psi\rangle_t = a_g(t)\,|g\rangle + a_1(t)\,|1\rangle + a_2(t)\,|2\rangle$$
$$+ \sum_k \int dE \, a_{Ek}(t)\,|Ek\rangle ,$$
(6)

where the $a_i(t)$ are the interaction picture probability amplitudes. The index k in the sum of continuum states ac-

counts for multiple ionization continua. The probability amplitudes are solved using the Fourier expansion[23]

$$a_i(t) = \sum_{n=-\infty}^{\infty} a_i^{(n)}(t) e^{-in\omega_L t}$$
(7)

to remove the explicit time dependence of the perturbation (equivalent to the rotating-wave approximation). The series is solved iteratively with the initial condition $|\psi\rangle_{t=0} = |g\rangle$ to yield the following recursion relation for the harmonic amplitudes $a_i^{(n)}(t)$:

$$i\hbar \dot{a}_i^{(n)}(t) = (E_i - n\hbar\omega_L)a_i^{(n)}(t)$$
$$- \sum_j \langle i | \boldsymbol{\mu} \cdot \mathscr{E}_0 | j \rangle a_j^{(n-1)}(t)$$
$$- \sum_j \langle i | \boldsymbol{\mu} \cdot \mathscr{E}_0^* | j \rangle a_j^{(n+1)}(t) .$$
(8)

(The sum over dipole-allowed intermediate states $|j\rangle$ is understood to include continuum states as well.) The series solution of Eq. (7) is truncated to a few terms since $a_g^{(0)}(t)$, $a_1^{(2)}(t)$, and $a_2^{(2)}(t)$ are expected to be the only large amplitudes. Use of the ansatz

$$a_j^{(n)}(t) = \bar{a}_j^{(n)}(t) e^{-iE_g t/\hbar}$$
(9)

gives

$$\left[i\hbar \frac{d}{dt} + E_g - \hbar\omega_L - E_j\right]\bar{a}_j^{(-1)}(t)$$
$$= -\langle j | \boldsymbol{\mu} \cdot \mathscr{E}_0^* | g \rangle \bar{a}_g^{(0)}(t) ,$$
(10a)

$$\left[i\hbar \frac{d}{dt} + E_g + \hbar\omega_L - E_j\right]\bar{a}_j^{(+1)}(t)$$
$$= -\langle j | \boldsymbol{\mu} \cdot \mathscr{E}_0 | g \rangle \bar{a}_g^{(0)}(t)$$
$$- \langle j | \boldsymbol{\mu} \cdot \mathscr{E}_0^* | 1 \rangle \bar{a}_1^{(2)}(t) - \langle j | \boldsymbol{\mu} \cdot \mathscr{E}^* | 2 \rangle \bar{a}_2^{(2)}(t) ,$$
(10b)

TABLE II. $\Delta J = 2$ resonance positions and integrated ion yield: linear polarization, $I_0 \approx 1.1$ GW/cm^2.

Designation	Peak position, $2\bar{\nu}_L$ (± 0.15 cm^{-1})	Integrated MPI rate[a] (rel. units)
$6s\,17d\ ^3D_2$	b	0.125
$^1D_2$	b	1.44
$6s\,18d\ ^3D_2$	41 560.7	0.11
$^1D_2$	41 566.9	1.39
$6s\,19d\ ^3D_2$	41 617.25	0.13
$^1D_2$	41 622.2	1.25
$6s\,20d\ ^3D_2$	41 664.25	0.135
$^1D_2$	41 668.2	1.20
$6s\,21d\ ^3D_2$	41 703.9	0.18
$^1D_2$	41 707.1	1.11
$6s\,22d\ ^3D_2$	41 737.1	0.11
$^1D_2$	41 739.8	1.00
$6s\,23d\ ^3D_2$	41 766.3	
$^1D_2$	41 768.2	1.00[c]
$6s\,24d\ ^3D_2$	41 790.7	
$^1D_2$	41 792.5	1.03[c]
$6s\,25d\ ^3D_2$	41 811.4	
$^1D_2$	41 812.9	0.98[c]
$6s\,26d\ ^3D_2$	41 828.8	
$^1D_2$	41 831.4	1.00[c]
$5d\,7d\ ^1D_2$	41 841.0	0.435
$6s\,27d\ ^3D_2$	41 847.4	0.12
$^1D_2$	41 851.3	0.07
$6s\,28d^{3,1}D_2$	41 864.0	0.36[c]
$5d\,7d\ ^3P_2$	41 867.95	0.01[c]
$6s\,29d^{3,1}D_2$	41 876.3	0.35[c]
$6s\,30d^{3,1}D_2$	41 887.3	0.34[c]
$6s\,31d^{3,1}D_2$	41 897.5	0.30[c]
$6s\,32d^{3,1}D_2$	41 906.6	
$6s\,33d^{3,1}D_2$	41 914.9	
$6s\,34d^{3,1}D_2$	41 922.4	
$6s\,35d^{3,1}D_2$	41 929.2	
$6s\,36d^{3,1}D_2$	41 935.5	

[a]Normalized with respect to the $6s\,22d\ ^1D_2$ resonance.
[b]OGE spectra were not available for calibration.
[c]Values are given for entire multiplet since the resonances were not fully resolved.

$$\left[i\hbar \frac{d}{dt} + E_g + 3\hbar\omega_L - E_j \right] \bar{a}_j^{(3)}(t)$$

$$= -\langle j \mid \boldsymbol{\mu} \cdot \boldsymbol{\mathscr{E}}_0 \mid 1 \rangle \bar{a}_1^{(2)}(t) - \langle j \mid \boldsymbol{\mu} \cdot \boldsymbol{\mathscr{E}}_0 \mid 2 \rangle \bar{a}_2^{(2)}(t) \qquad (10c)$$

for the time development of the intermediate-state amplitudes. It is assumed that $\boldsymbol{\mathscr{E}}_0(t)$, $\bar{a}_g^{(0)}(t)$, and $\bar{a}_{1,2}^{(2)}(t)$ are slowly varying in comparison to the energy differences $E_g + \hbar\omega_L - E_j$, etc., since the latter are $\gtrsim 10^{13}$ sec^{-1} for the levels considered.

Equations (10a)—(10c) are then integrated formally and substituted into Eqs. (8a)—(8c) for the even-parity state amplitudes. Only terms with low-frequency modulation are retained to give an effective Hamiltonian for the in-

TABLE III. $\Delta J = 2$ resonance positions and integrated ion yield; circular polarization, $I_0 \approx 1.1$ GW/cm^2.

Designation	Peak position, $2\bar{\nu}_L$ (± 0.15 cm^{-1})	Integrated MPI rate[a] (rel. units)
$6s\,17d\ ^3D_2$	b	0.82
$^1D_2$	b	1.64
$6s\,18d\ ^3D_2$	41 560.3	0.53
$^1D_2$	41 567.1	1.83
$6s\,19d\ ^3D_2$	41 616.9	0.45
$^1D_2$	41 622.5	1.04
$6s\,20d\ ^3D_2$	41 663.5	0.53
$^1D_2$	41 668.6	1.00
$6s\,21d\ ^3D_2$	41 703.1	0.50
$^1D_2$	41 707.4	0.78
$6s\,22d\ ^3D_2$	41 736.4	0.49
$^1D_2$	41 740.15	0.70
$6s\,23d\ ^3D_2$	41 764.9	0.51
$^1D_2$	41 768.3	0.64
$6s\,24d\ ^3D_2$	41 789.6	0.41
$^1D_2$	41 792.65	0.62
$6s\,25d\ ^3D_2$	41 810.8	0.49
$^1D_2$	41 813.4	0.47
$6s\,26d\ ^3D_2$	41 828.5	0.64
$^1D_2$	41 831.8	0.32
$5d\,7d\ ^1D_2$	41 840.8	0.48
$6s\,27d\ ^3D_2$	41 847.9	0.11
$^1D_2$	41 850.6	0.12

teraction of the even-parity levels as

$$\frac{d}{dt}\bar{a}\,_g^{(0)}(t) = -i\Omega_{1g}\bar{a}\,_1^{(2)}(t) - i\Omega_{2g}\bar{a}\,_2^{(2)}(t) \ , \tag{11a}$$

$$\left[\frac{d}{dt} - i\Delta + \gamma_{11}\right]\bar{a}\,_1^{(2)}(t)$$

$$= -i(\delta\omega_{12} - i\gamma_{12})\bar{a}\,_2^{(2)}(t) - i\Omega_{1g}\bar{a}\,_g^{(0)}(t) \ , \tag{11b}$$

$$\left[\frac{d}{dt} - i(\Delta + \delta) + \gamma_{22}\right]\bar{a}\,_2^{(2)}(t)$$

$$= -i(\delta\omega_{12} - i\gamma_{12})\bar{a}\,_1^{(2)}(t) - i\Omega_{2g}\bar{a}\,_g^{(0)}(t) \ . \tag{11c}$$

The terms are identified below. The three resonant levels experience light shifts given as

$$\hbar\delta\omega_g = \sum_j \left[\frac{\langle g\,|\,\boldsymbol{\mu}\cdot\boldsymbol{\mathscr{E}}_0\,|\,j\rangle\langle j\,|\,\boldsymbol{\mu}\cdot\boldsymbol{\mathscr{E}}_0^*\,|\,g\rangle}{E_g - \hbar\omega_L - E_j} \right.$$

$$\left. + \frac{\langle g\,|\,\boldsymbol{\mu}\cdot\boldsymbol{\mathscr{E}}_0^*\,|\,j\rangle\langle j\,|\,\boldsymbol{\mu}\cdot\boldsymbol{\mathscr{E}}_0\,|\,g\rangle}{E_g + \hbar\omega_L - E_j} \right] \ , \tag{12}$$

$$\hbar\delta\omega_{11} = P \left[\sum_j \frac{\langle 1\,|\,\boldsymbol{\mu}\cdot\boldsymbol{\mathscr{E}}_0^*\,|\,j\rangle\langle j\,|\,\boldsymbol{\mu}\cdot\boldsymbol{\mathscr{E}}_0\,|\,1\rangle}{E_g + 3\hbar\omega_L - E_j} \right.$$

$$\left. + \sum_j \frac{\langle 1\,|\,\boldsymbol{\mu}\cdot\boldsymbol{\mathscr{E}}_0\,|\,j\rangle\langle j\,|\,\boldsymbol{\mu}\cdot\boldsymbol{\mathscr{E}}_0^*\,|\,1\rangle}{E_g + \hbar\omega_L - E_j} \right] \tag{13}$$

and similarly for $\delta\omega_{22}$ with the appropriate indices switched. The sums include a Cauchy principal part integral, denoted by P, of odd-parity continuum states. These level shifts are incorporated into the effective equations of motion with the identities

$$\hbar\Delta \equiv E_g + \hbar\delta\omega_g + 2\hbar\omega_L - E_1 - \hbar\omega_{11} \ ,$$

$$\hbar\delta \equiv E_1 + \hbar\delta\omega_{11} - E_2 - \hbar\delta\omega_{22} \ .$$

The two-photon Rabi rates Ω_{ig} to states $|1\rangle$ and $|2\rangle$ are given as

$$\hbar\Omega_{ig} = \sum_j \frac{\langle i\,|\,\boldsymbol{\mu}\cdot\boldsymbol{\mathscr{E}}_0\,|\,j\rangle\langle j\,|\,\boldsymbol{\mu}\cdot\boldsymbol{\mathscr{E}}_0\,|\,g\rangle}{E_g + \hbar\omega_L - E_j} \ . \tag{14}$$

TABLE III. (*Continued*).

Designation	Peak position, $2\bar{\nu}_L$ (± 0.15 cm^{-1})	Integrated MPI rate[a] (rel. units)
$6s\,28d\;^3D_2$		0.02
$^1D_2$	41 863.9	0.24
$6s\,29d\;^3D_2$		0.04
$^1D_2$	41 876.6	0.23
$6s\,30d\;^3D_2$		0.09
$^1D_2$	41 887.7	0.19
$6s\,31d\;^3D_2$		0.08
$^1D_2$	41 897.9	0.17
$6s\,32d\;^3D_2$		0.08
$^1D_2$	41 906.95	0.155
$6s\,33d\;^3D_2$		
$^1D_2$	41 915.3	
$6s\,34d\;^3D_2$		
$^1D_2$	41 922.9	
$6s\,35d\;^3D_2$		
$^1D_2$	41 929.7	
$6s\,36d\;^3D_2$		
$^1D_2$	41 936.05	
$6s\,37d\;^3D_2$		
$^1D_2$	41 941.8	
$6s\,38d\;^3D_2$		
$^1D_2$	41 947.25	

[a]Normalized with respect to the $6s\,22d\;^1D_2$ resonance (linear polarization).
[b]OGE spectra were not available for calibration.

The (half) rates for photoionization out of these states are

$$\hbar\gamma_{ii}=\pi\sum_k |\,\langle Ek\,|\,\boldsymbol{\mu}\cdot\boldsymbol{\mathscr{E}}_0\,|\,i\,\rangle\,|_{E=E_g+3\hbar\omega_L}^2 \;. \qquad (15)$$

This is recognized simply as Fermi's golden rule where the density of final states is incorporated in the matrix element by requiring an energy normalization of the continuum wave functions. Two additional terms $\delta\omega_{12}$ and γ_{12}, similar in form to Raman scattering amplitudes, are given as

$$\hbar\delta\omega_{12}=P\left[\sum_j \frac{\langle 1\,|\,\boldsymbol{\mu}\cdot\boldsymbol{\mathscr{E}}_0^*\,|\,j\,\rangle\langle j\,|\,\boldsymbol{\mu}\cdot\boldsymbol{\mathscr{E}}_0\,|\,2\,\rangle}{E_g+3\hbar\omega_L-E_j}\right.$$

$$\left. +\sum_j \frac{\langle 1\,|\,\boldsymbol{\mu}\cdot\boldsymbol{\mathscr{E}}_0\,|\,j\,\rangle\langle j\,|\,\boldsymbol{\mu}\cdot\boldsymbol{\mathscr{E}}_0^*\,|\,2\,\rangle}{E_g+\hbar\omega_L-E_j}\right], \qquad (16)$$

$$\hbar\gamma_{12}=\pi\sum_k \langle 1\,|\,\boldsymbol{\mu}\cdot\boldsymbol{\mathscr{E}}_0^*\,|\,Ek\,\rangle\langle Ek\,|\,\boldsymbol{\mu}\cdot\boldsymbol{\mathscr{E}}_0\,|\,2\,\rangle\,|_{E=E_g+3\hbar\omega_L} \;.$$

$$(17)$$

The real quantity of the Raman coupling $\delta\omega_{12}$ is interpreted as a scattering amplitude through bound levels, the first term of which predominantly weights contributions due to autoionization levels such as $6pnd\;J^\pi=1^-$ and/or 3^- for linear or circular polarization. The second quantity, γ_{12}, is the imaginary scattering amplitude through continuum states. In the special case of one continuum, the latter quantity reduces to

$$\gamma_{12}=\sqrt{\gamma_{11}}\sqrt{\gamma_{22}} \;. \qquad (18)$$

We introduce a new parameter q which measures the coupling of the near-resonant intermediate states in terms of the signed ratio

$$q\equiv\delta\omega_{12}/\gamma_{12} \;. \qquad (19)$$

The rate of three-photon ionization $\Gamma(t)$ is given formally as

$$\Gamma(t) = \frac{d}{dt} P_{\text{ion}} = -2 \operatorname{Re}[(\bar{a}_g^{(0)*} \dot{\bar{a}}_g^{(0)}) + (\bar{a}_1^{(2)*} \dot{\bar{a}}_1^{(2)})$$

$$+ (\bar{a}_2^{(2)*} \dot{\bar{a}}_2^{(2)})] \ . \qquad (20a)$$

This can be rewritten in a more recognizable form using Eqs. (11a)—(11c) to give

$$\Gamma(t) = \frac{2\pi}{\hbar} [\gamma_{11} |\bar{a}_1^{(2)}(t)|^2 + \gamma_{22} |\bar{a}_2^{(2)}(t)|^2$$

$$+ 2 \operatorname{Re}(\gamma_{12} \bar{a}_1^{(2)*} \bar{a}_2^{(2)})] \ . \qquad (20b)$$

When there is only one continuum available for ionization this reduces to

$$\Gamma(t) = \frac{2\pi}{\hbar} | \sqrt{\gamma_{11}} \bar{a}_1^{(2)}(t) + \sqrt{\gamma_{22}} \bar{a}_2^{(2)}(t) |^2 \ . \qquad (20c)$$

The latter two forms for the rate of MPI indicate more clearly that channel interference will take place between the near-resonant states $|1\rangle$ and $|2\rangle$.

A. Circular polarization

In succeeding sections, model calculations are provided using Eq. (20c) for the rate of MPI with circularly polarized light. The intermediate resonant-state amplitudes are obtained using the approximation $\bar{a}_g^{(0)} \approx 1$ for all times and assuming there is a stationary-state case with $\dot{\bar{a}}_i^{(2)}(t) \ll \gamma_{ii} \bar{a}_i^{(2)}$, etc. This yields the following solutions for the resonant amplitudes:

$$\bar{a}_1^{(2)} = \frac{(\Delta + \delta + i\gamma_{22})\Omega_{1g} + (\delta\omega_{12} - i\gamma_{12})\Omega_{2g}}{D} \ , \qquad (21a)$$

$$\bar{a}_2^{(2)} = \frac{(\Delta + i\gamma_{11})\Omega_{2g} + (\delta\omega_{12} - i\gamma_{12})\Omega_{1g}}{D} \ , \qquad (21b)$$

$$D = (\Delta + i\gamma_{11})(\Delta + \delta + i\gamma_{22}) - |\delta\omega_{12}|^2 + |\gamma_{12}|^2$$

$$+ 2i \operatorname{Re}(\gamma_{12}\delta\omega_{12}) \ . \qquad (21c)$$

These solutions do not account for depletion of the ground state. More significantly, the validity of a stationary-state approximation is questionable for the case of two-photon resonant, three-photon ionization if $\gamma_{ii} \approx \Omega_{ig}$. It will be shown, however, that these restrictive solutions do yield model profiles which reasonably approximate experimental data and that the salient features can be understood in terms of a few parameters.

B. Linear polarization

Evidence of interference is expected to be less pronounced for the case of linear polarization because there are two incoherent pathways to ionization. As a result, an additional set of final-state probability amplitudes a_{EJ} must be solved to yield a total ionization rate Γ_T of the form

$$\Gamma_T \propto \sum_{J=1,3} \frac{d}{dt} \int dE \, |a_{EJ}|^2 \ . \qquad (22)$$

A detailed analysis of the MPI profiles in terms of Eq. (22) will be left to later work. Instead, analysis of the profiles is given by a rate-equation formulation for an isolated resonance since interference effects are not evident in the data. The MPI rate $\Gamma^{(2+1)}$ is given in terms of the two-photon Rabi rate $\Omega_{ig}^{(2)}$ of the bound-bound transition and the excited-state photoionization rate γ_r as[4]

$$\Gamma^{(2+1)}(\Delta) = \frac{(\Omega^{(2)})^2}{4} \gamma_r \frac{\Gamma_t/\Gamma_l}{(\omega_{ig} - 2\omega_L + S_{ig})^2 + (\Gamma_t/2)^2 + (\Omega^{(2)})^2 \Gamma_t/\Gamma_l} \ . \qquad (23)$$

V. MODEL CALCULATIONS

A. Effective matrix elements; circular polarization

Estimates for the effective operators of Eqs. (11a)—(11c) are calculated using empirical values for the transition matrix elements based on lifetime and oscillator strength data. This is done by making use of the relation

$$|\langle \alpha' J' M' | e \mathbf{r} \cdot \hat{e} | \alpha J M \rangle|^2$$

$$= \begin{bmatrix} J' & 1 & J \\ -M' & K & M \end{bmatrix}^2 \frac{3}{2} \frac{\hbar e^2}{m_e} \frac{2J+1}{\omega_{JJ'}} f(J, J') \ ,$$

where $f(J, J')$ is the absorption oscillator strength from state J to J'.

As noted in the Introduction, the resonance condition Δ for the bound-bound transition is modified to include the set quadratic shift S_{rg} of the bound levels. The transverse relaxation rate Γ_t due to phase-changing processes is taken as

$$\Gamma_t \approx A + \gamma_L + \gamma_r \ . \qquad (24)$$

Here A is the spontaneous radiative decay of the excited state, and γ_L represents the effective linewidth of the two-photon transition due to the laser bandwidth ($\gamma_L \approx 2b$ for a chaotic field). The longitudinal rate of relaxation Γ_l includes all processes which affect the population of the resonant state and is taken to be

$$\Gamma_l \approx A + \gamma_r \ . \qquad (25)$$

1. Quadratic shifts

The ground-state shift $\bar{\nu}_g$ ($=\delta\omega_g/2\pi c$) takes the form

$$\bar{\nu}_g = 1.13\times10^8 \sum_j \frac{1}{3}\frac{f_{gj}}{\sigma_{jg}} \left| \frac{1}{\sigma_L-\sigma_{jg}} + \frac{1}{\sigma_{jg}+\sigma_L} \right| I(\text{GW/cm}^2)\ \text{cm}^{-1},$$

(26)

where σ_L is the laser frequency and σ_{jg} is the field-free spacing between the ground and intermediate electric-dipole-allowed states, both in wave numbers. The series is truncated to include only those levels given in Table IV. For the situation of a laser tuned near the $6s\,22d$ $J=2$ doublet, $\bar{\nu}_g \approx 1.05$ cm^{-1} (GW/cm$^2)^{-1}$. Effects of the unaccounted $J^\pi=1^-$ states should amount to less than a 2% reduction of this value since 98% of the total valence oscillator strength is accounted for by the first six levels.

Evaluation of the near-resonant intermediate-state shifts proceeds similarly except there is the necessity to include odd-parity autoionization levels. The principal part integral of the first term of Eq. (13) weights virtual transitions between the $6snd$ $J^\pi=2^+$ bound levels and doubly excited $J^\pi=3^-$ levels near the $6p_{1/2,3/2}$ ionization limits. It is estimated by assuming the dominant matrix elements involve virtual transitions between the $6snd$ and $6pnd$ levels since it has been shown that f values for these transitions are comparable, respectively, to the $6s_{1/2}$-$6p_{1/2,3/2}$ ionic transitions of $\frac{1}{3}$ and $\frac{2}{3}$.[11] These matrix elements are calculated using coupling formulas for reduced matrix elements between two-electron wave functions and assume like Ref. 11 that the transition proceeds between the core electrons. The second term in Eq. (13) weights virtual transitions to $J^\pi=1^-$ bound states and its effect is expected to be negligible by comparison since $f(6s\,6p\ ^1P_1^\circ-6snd\ J=2)\leq5\times10^{-3}$ for $n\geq16$ (based on lifetime data of Ref. 24). Possible exceptions to this are $6snd$ states with large admixture of the $5d\,7d\ ^1D_2$ state which radiatively decay at rates $\sim5\times10^6$ sec^{-1}. This would yield a maximum red shift ~0.07 cm^{-1} (GW/cm^2) if this were all due to the $5d\,6p\ ^3D_1^\circ$ state (and smaller still if the total radiative rate is spread over all $5d\,6p\ ^3J^\pi=1^-$ states).

The influence of the second term in Eq. (13) (including the principal part contribution) is neglected and the

TABLE IV. Bound $J^\pi=1^-$ intermediate states used to calculate $\bar{\nu}_g$.

Designation	Level position (cm^{-1})	Absorption f values[a]
$6s\,6p\ ^3P_1^\circ$	12 636.6	0.01
$6s\,6p\ ^1P_1^\circ$	18 060.3	1.59
$5d\,6p\ ^3D_1^\circ$	24 192.1	0.01
$5d\,6p\ ^3P_1^\circ$	25 704.1	0.01
$5d\,6p\ ^1P_1^\circ$	28 554.3	0.16
$6s\,7p\ ^1P_1^\circ$	32 547.1	0.17

[a]Reference 13.

excited-state quadratic shifts $\bar{\nu}_{ii}$ ($\equiv\delta\omega_{ii}/2\pi c$) take the approximate form

$$\bar{\nu}_{ii} \approx 2.26\times10^8 \left| \frac{0.667}{21\,952} \sum_{s=1}^{2} \frac{j_s}{\sigma_{Ls}} + \frac{0.333}{20\,261}\frac{j_3}{\sigma_{L3}} \right| I(\text{GW/cm}^2)\ \text{cm}^{-1}.$$

(27)

The terms are due to virtual transitions to the $J^\pi=3^-$ levels belonging to the $6p_{3/2}nd_{3/2,5/3}$ series and the $6p_{1/2}nd_{5/2}$ series. The energy detunings are denoted $\sigma_{Ls}\equiv3\bar{\nu}_L-\bar{\nu}_{sg}$ (cm^{-1}). The j_s terms are angular factors which are sensitive to the amount of singlet-triplet mixing of the $6snd$ $J=2$ doublet.

Previous work indicates this mixing is such that

$$|2\rangle = \alpha\,|\,6snd\ ^1D_2\rangle + \beta\,|\,6snd\ ^3D_2\rangle + \gamma\,|\,5d\,7d\ ^1D_2\rangle\ ,$$

$$|1\rangle = -\beta\,|\,6snd\ ^1D_2\rangle + \alpha\,|\,6snd\ ^3D_2\rangle + \gamma'\,|\,5d\,7d\ ^1D_2\rangle$$

with $|\beta|\leq0.16$ for $n\geq16$.[25,26] For this work we choose to rewrite the $|\,6snd\rangle$ part of the wave functions in terms of jj basis states:

$$|2\rangle = B\,|\,1/2,5/2\rangle + A\,|\,1/2,3/2\rangle + \gamma\,|\,5d\,7d\ ^1D_2\rangle\ ,$$

(28a)

$$|1\rangle = A\,|\,1/2,5/2\rangle - B\,|\,1/2,3/2\rangle + \gamma'\,|\,5d\,7d\ ^1D_2\rangle\ ,$$

(28b)

where

$$A = \alpha\sqrt{2/5} - \beta\sqrt{3/5}\ ,$$

(29a)

$$B = \alpha\sqrt{3/5} + \beta\sqrt{2/5}\ .$$

(29b)

Similarly, the $6pnd$ $J=3$ levels are taken to be

$$|J^{(1)}=3\rangle = A'\,|\,3/2,5/2\rangle + B'\,|\,3/2,3/2\rangle\ ,$$

(30a)

$$|J^{(2)}=3\rangle = -B'\,|\,3/2,5/2\rangle + A'\,|\,3/2,3/2\rangle\ ,$$

(30b)

$$|J^{(3)}=3\rangle = 1\,|\,1/2,5/2\rangle\ .$$

(30c)

Values of $A'=0.900$ and $B'=0.436$ were assigned so that the calculated ratio of line strengths

$$\frac{|\langle j^{(1)}|r|2\rangle|^2}{|\langle j^{(2)}|r|2\rangle|^2} \approx 15{:}1$$

for $16\leq n<22$ in accordance with recent measurements.[11(b)] The angular terms are calculated from standard coupling formulas for reduced matrix elements[27] which give

$$|\langle 6p_{3/2}nd\ j^{(i)}=3\,|\,r\,|\,6s_{1/2}nd\ J^{(1)}=2\rangle|^2$$

$$\rightarrow j_i^{(1)}\,|\langle 6p_{3/2}||r||6s_{1/2}\rangle|^2$$

or

$$|\langle 6p_{1/2}nd\ J^{(3)}=3\,|\,r\,|\,6s_{1/2}nd\ J^{(1)}=2\rangle|^2$$

$$\rightarrow j_3^{(1)}\,|\langle 6p_{1/2}||r||6s_{1/2}\rangle|^2$$

with

TABLE V. Calculated effective matrix elements with $I = 1$ GW/cm^2.

η	$\bar{v}_g$ (cm^{-1})	$\bar{v}_{11}$ (cm^{-1})	$\bar{v}_{22}$ (cm^{-1})	$\bar{v}_{12}$ (cm^{-1})	γ_{11} (cm^{-1})	γ_{22} (cm^{-1})	γ_{12} (cm^{-1})	q
16	1.11	−0.62	+0.95	+1.35	0.08	0.11	+0.04	+27
20	1.05	−1.04	+0.62	+1.06	0.01	0.01	−0.004	−265
22	1.04	−1.23	+0.64	+0.88	0.03	0.01	−0.004	−220
		−1.14[a]	+0.55[a]	+0.96[a]			−0.004[a]	−220[a]
24	1.03	−1.49	+0.78	+0.80	0.03	0.001	+0.002	+400
		−1.25[a]	+0.54[a]	+0.87[a]			−0.002[a]	−400[a]
25	1.02	−1.57	+0.77	−0.57	0.007	0.005	−0.004	+150
		−1.49[a]	+0.73[a]	+0.53[a]			−0.004[a]	−150[a]
26	1.02	+0.57	−1.28	+0.62	0.004	0.007	+0.002	+310
		−1.33[a]	+0.62[a]	−0.49[a]			−0.002[a]	+250[a]
27	1.01	−0.04	−0.66	+0.96	3×10^{-4}	0.003	-7×10^{-5}	-1×10^4
		+0.36[a]	−1.05[a]	+0.72[a]			-2×10^{-5}[a]	-4×10^{4}[a]
28	1.01	−0.37	−0.48	+1.18	0.003	0.003	−0.001	−1200
		−0.26[a]	−0.58[a]	+1.17[a]			−0.001[a]	−1200[a]
40	0.99	−1.14	+0.03	+1.06	1×10^{-4}	5×10^{-5}	-4×10^{-5}	−2800

[a]Values based on β from Table VI. Other values based on β from Ref. 26.

$$j_1^{(1)} = \left[\frac{AA'}{3} - \frac{BB'}{2} \right], \tag{31a}$$

$$j_2^{(1)} = \left[\frac{AB'}{3} + \frac{BA'}{2} \right], \tag{31b}$$

$$j_3^{(1)} = \tfrac{5}{18} A^2 \tag{31c}$$

and, similarly, for state $|2\rangle$, with

$$j_1^{(2)} = \left[\frac{BA'}{3} + \frac{AB'}{2} \right]^2, \tag{32a}$$

$$j_2^{(2)} = \left[\frac{BB'}{3} - \frac{AA'}{2} \right]^2, \tag{32b}$$

$$j_3^{(2)} = \tfrac{5}{18} B^2 . \tag{32c}$$

Calculated values for the quadratic shifts are given in Table V. The first set of calculated shifts is based on values of β obtained from hfs measurements.[26] It was noted that these values do *not* reproduce observed photoabsorption ratios[28]

$$R \equiv \frac{|\langle 6snd \ J^{(2)} = 2 | r | 6s \ 6p \ ^1P_1^\circ \rangle |^2}{|\langle 6snd \ J^{(1)} = 2 | r | 6s \ 6p \ ^1P_1^\circ \rangle |^2}$$

for principal quantum numbers n near the $5d\,7d\ ^1D_2$ perturber. The second set of calculated shifts is based on values of β used to match the photoabsorption data. Table VI gives values of R and the recalculated α and β

coefficients based on the photoabsorption measurements of Ref. 28. These calculated line strength ratios assume

$$| 6s \ 6p \ ``^1P_1^\circ" \rangle = \alpha' | 6s \ 6p \ ^1P_1^\circ \rangle + \beta' | 6s \ 6p \ ^3P_1^\circ \rangle$$

$$= A'' | 1/2, 3/2 \rangle + B'' | 1/2, 1/2 \rangle ,$$

$$A'' = \alpha' \sqrt{2/3} - \beta' \sqrt{1/3}, \quad B'' = \alpha' \sqrt{1/3} + \beta' \sqrt{2/3}$$

with $\beta' = 0.107$. This value was chosen by assuming the assignment of β (Ref. 26) for the $6s\,20d\ J = 2$ doublet is correct and then fitting A'' and B'' to the photoabsorption data.

TABLE VI. Singlet-triplet mixing coefficients α and β based on relative f values $R = f(6s\,6p\ ^1P_1^\circ - 6snd\ ^1D_2)/f(6s\,6p\ ^1P_1^\circ - 6snd\ ^3D_2)$.

n	R[a]	γ^2[b]	α	β
20	27.0	0.007	0.9709	0.225
22	19.0	0.008	0.9624	0.2565
24	14.0	0.013	0.9498	0.2914
25	5.0	0.018	0.8876	0.4407
26	0.69	0.125	0.5692	0.7423
27	3.0	0.189	0.7956	−0.4219
28	23.0	0.048	0.9619	−0.1635

[a]Reference 28.
[b]Reference 26.

2. Rabi rates

The two-photon Rabi rates $\overline{\Omega}_{ig}$ ($\equiv \Omega_{ig}/2\pi c$) are calculated by considering only the contribution of the $6s\,6p\,{}^1P_1^\circ$ level to the sum in Eq. (14). Thus

$$\overline{\Omega}_{ig} \approx 1.13 \times 10^8 \left[\frac{1.59}{18\,060} 3 \frac{f_{1i}}{\sigma_{i1}} \right]^{1/2}$$

$$\times \begin{bmatrix} J_1 & 1 & J_g \\ -M_1 & \kappa & 0 \end{bmatrix} \begin{bmatrix} J_2^{(i)} & 1 & J_1 \\ -M_2 & \kappa & M_1 \end{bmatrix}$$

$$\times \left[\frac{1}{\sigma_L - 18\,060} \right] I(\text{GW/cm}^2)\ \text{cm}^{-1}, \qquad (33)$$

where f_{1i} is the absorption oscillator strength for the $(6s\,6p\,{}^1P_1^\circ) \rightarrow (6snd\ J^{(i)}=2)$ transition, σ_{i1} is the wavenumber difference for this transition, and there is the usual wave-number detuning between the laser and intermediate state. The 3-j coefficients account for effects of light polarization with $\kappa = \pm 1$ and 0 for circular and linear polarization. It is noted that

$$(\Omega_{\text{cir}}^{(2)}/\Omega_{\text{lin}}^{(2)})^2 = \tfrac{5}{3}$$

because of the second 3-j coefficient.

Experimental values of $f_{1i}(6s\,6p\,{}^1P_1^\circ \rightarrow 6snd\ J^{(i)}=2)$ do not exist, so upper bounds for these values are inferred from lifetime data[24] assuming the radiative transitions were entirely to the $6s\,6p\,{}^1P_1^\circ$ level. This yields

$$f({}^1P_1^\circ \equiv 6snd\ J^{(2)}=2) \sim 3.6 \times 10^{-3} \left[\frac{19.25}{v_n^*} \right]^3, \qquad (34)$$

where v_n^* is the effective quantum number of the $6snd$ levels. Values of v_n^* are determined in the usual way from

$$E_n = I(6s_{1/2}) - \frac{R_{\text{Ba}}}{(v_n^*)^2}, \qquad (35)$$

where $I(6s_{1/2}) = 42\,035.0\ \text{cm}^{-1}$ and $R_{\text{Ba}} = 109\,736.9\ \text{cm}^{-1}$. For the case of circular polarization, $\overline{\Omega}_{2g}(n=22) \sim 0.055\ \text{cm}^{-1}$ and $\overline{\Omega}_{1g}(22) \approx (\beta/\alpha)\overline{\Omega}_{2g}(22) \approx 0.015\ \text{cm}^{-1}$.

3. Photoionization rates

The photoionization (half) rate $\overline{\gamma}_{11}$ ($\equiv \gamma_{11}/2\pi c$) and $\overline{\gamma}_{22}$ were calculated from the relation

$$\gamma_{ii} = \frac{\sigma_{ii} F(\text{photons/cm}^2\,\text{sec})}{2}\ \text{sec}^{-1}, \qquad (36)$$

where the cross sections σ_{ii} are given by[29]

$$\sigma_{ii} = \frac{4\pi}{137} \omega_L \sum_s |\langle \Psi_s^\varepsilon | r | i \rangle|^2\ \text{a.u.}, \qquad (37a)$$

$$\sigma_{ii} = \sigma(\text{a.u.}) r_B^2\ \text{cm}^2. \qquad (37b)$$

The sum accounts for contributions from the different $J^\pi = 3^-$ series. The calculations of Eq. (37a) follow that of Ref. 30 with a few modifications. The final-state wave functions Ψ_s^ε (energy normalized) are written as a linear combination of a discrete state $\phi_{\varepsilon,s}$ and one continuum state ψ_ε as

$$\Psi_s^\varepsilon = a_s^\varepsilon \phi_{\varepsilon,s} + \int b_{\varepsilon'}^\varepsilon \psi_{\varepsilon'} d\varepsilon. \qquad (38)$$

Unlike Ref. 30, we omit the factor v_ε^3 in the first term since the coefficients a and b are already energy normalized.[31] In this work, the discrete states ϕ_s ($6pnd\ J^{(s)} = 3$) are represented with the jj coupling scheme using Eqs. (30a)–(30c). Absorption occurs predominantly to the discrete state so the energy dependence of the line strength is taken to be[11(a),31]

$$(a_{s,p}^\varepsilon)^2 = \sum_p \frac{V_s^2/v_p^3}{(3\hbar\omega_L - \varepsilon_{s,p})^2 + (\pi V_s/v_p^3)^2}, \qquad (39)$$

where $3\varepsilon_L - \varepsilon_{s,p}$ is the three-photon laser detuning (in rydbergs) from the autoionization peaks. The discrete-continuum interaction energy of the Ba $6pnd\ J^\pi = 3^-$ autoionization profiles is[11]

$$2\pi V_s^2 \sim 0.11\ \text{Ry}.$$

Values of $v_{s,p}$ are given by the relation $v_{s,p} = p - \delta_s$ where $\delta_1 \approx 2.739$ [Ref. 11(a)], $\delta_2 \approx 2.894$ [Ref. 11(b)], and $\delta_3 \approx 2.760$ [Ref. 11(b)], and the $\varepsilon_{s,p}$ are calculated from Eq. (35) with $I(6p_{1/2}) = 62\,296.6\ \text{cm}^{-1}$ and $I(6p_{3/2}) = 63\,987.4\ \text{cm}^{-1}$.

Following Ref. 30, transition matrix elements of the form $\langle 6pn'(\approx v_\varepsilon)l'\ J' | r | 6snl\ J \rangle$ are reduced as

$$\langle \alpha_1' j_1' \alpha_2' j_2' J' | r | \alpha_1 j_1 \alpha_2 j_2 J \rangle$$

$$= \begin{bmatrix} J' & 1 & J \\ -M_J & K & M_J \end{bmatrix} (-1)^{j_1' + j_2' + J + 1}$$

$$\times [(2J+1)(2J'+1)]^{1/2} \begin{Bmatrix} j_1' & j_2' & J' \\ J & 1 & j_1 \end{Bmatrix}$$

$$\times \langle 6p(j_1') || r_1 || 6s_{1/2} \rangle \delta_{ll'} O(n,v_\varepsilon) \qquad (40)$$

with

$$O(n,v_\varepsilon) = 2 \frac{(v_n v_\varepsilon)^{1/2}}{v_\varepsilon + v_n} \frac{\sin[\pi(v_\varepsilon - v_n)]}{\pi(v_\varepsilon - v_n)}. \qquad (41)$$

This modification of the Kroenecker function $\delta_{n,n',l,l'} \rightarrow \delta_{ll'} O(n,v_\varepsilon)$ allows for readjustment of the Rydberg electron to new boundary conditions when the core electron makes a transition.[30] Values of the line strength $|\langle 6p_{1/2,3/2} || r || 6s_{1/2} \rangle|^2$ are taken to be, respectively, 11 and 22 (a.u.).[13]

The photoionization cross sections σ_{ii} from states $|1\rangle$ and $|2\rangle$ are calculated thus:

$$\sigma_{ii}=\frac{4\pi}{137}\omega_L(\text{a.u.})\left[\left[\sum_{s=1}^{2}(a_s^{\varepsilon})^2 j_s^{(1)}\right]O^2(n,\nu_\varepsilon(3/2))S(6s_{1/2}-6p_{3/2})+(a_{\frac{\varepsilon}{3}})^2 j_3^{(i)}O^2(n,\nu_\varepsilon(1/2))S(6s_{1/2}-6p_{1/2})\right]\text{a.u.}, \quad (42)$$

where the second term appears when $3\hbar\omega_L<\varepsilon(6p_{1/2})$. The angular factors $j_s^{(i)}$ are obtained from Eqs. (31) and (32). Values of $\overline{\gamma}_{ii}$ ($\equiv\gamma_{ii}/c$) are given in Table V for an incident intensity $I=1$ GW/cm^2 which corresponds to $F\sim2.4\times10^{27}$ (photons/cm^2 sec) at $\lambda_0\approx4800$ Å.

4. Raman coupling terms

The real part of the Raman coupling term $\overline{\nu}_{12}$ ($\equiv\delta\omega_{12}/2\pi c$) is evaluated like the quadratic shifts to give

$$\overline{\nu}_{12}=2.26\times10^8\left|\frac{0.667}{21\,952}\sum_s\frac{j_s^{(12)}}{\sigma_{Ls}}+\frac{0.333}{20\,261}\frac{j_3^{(12)}}{\sigma_{L3}}\right|I(\text{GW/cm}^2)\text{ cm}^{-1}. \quad (43)$$

The terms are interpreted analogously like those of Eq. (27) but the angular terms $j_s^{(12)}$ are

$$j_1^{(12)}=\left[\frac{AA'}{3}-\frac{BB'}{2}\right]\left[\frac{BA'}{3}+\frac{B'A}{2}\right],$$

$$j_2^{(12)}=-\left[\frac{AB'}{3}+\frac{BA'}{2}\right]\left[\frac{AA'}{2}-\frac{BB'}{3}\right],$$

$$j_3^{(12)}=\tfrac{5}{18}AB.$$

The imaginary term $\overline{\gamma}_{12}$ ($\equiv\gamma_{12}/2\pi c$) is evaluated like the photoionization rates where

$$\sigma_{12}=\frac{4\pi}{137}\omega_L(\text{a.u.})\left[\left[\sum_{s=1}^{2}(a_s^{\varepsilon})^2 j_s^{(12)}\right]O^2(n,\nu_\varepsilon(3/2))S(6s_{1/2}-6p_{3/2})+(a_{\frac{\varepsilon}{3}})^2 j_3^{(12)}O^2(n,\nu_\varepsilon(1/2))S(6s_{1/2}-6p_{1/2})\right]\text{a.u.} \quad (44)$$

Here the value of ν_n used in O^2 is taken to be that of state $|2\rangle$.

B. Model profiles, circular polarization

1. Plane-wave solutions

The influence of the real part of the Raman scattering amplitude, $\delta\omega_{12}$, is shown in Fig. 14. The results are obtained using Eq. (20c) and assuming a plane-wave distribution for the incident laser pulse. As noted previously, ω_{12} and γ_{12} are reexpressed by their signed ratio q. Three profiles are shown for the cases of $q=-10$, 0, and $+10$ which illustrate two characteristic effects of the Raman coupling. First, the effect of a nonzero q is analogous to that of a second-order perturbation; the resonant peaks are repelled with increasing $|q|$. Second, the sign of q affects the position of the interference node *and* the ratio of the peak heights; a negative value of q yields a ratio of the peak heights $\Gamma_{pk}(2)/\Gamma_{pk}(1)\sim(\Omega_{2g}/\Omega_{1g})^2\approx(\alpha/\beta)^2$. Positive values of q push the node nearer to the field-free position of state $|1\rangle$ and reduce $\Gamma_{pk}(1)$.

The peak positions are modified by the real part of the Raman coupling which acts in conjunction with the quadratic shift. The magnitude of the peak shifts for $|q|\neq0$ depends upon values of γ_{11} and γ_{22}, so the magnitude of peak shifts due to q is intensity dependent although q is not. This effect is illustrated in Fig. 15 for varying light intensities. It is notable that for this example $\overline{\nu}_g>\overline{\nu}_2$, so without a Raman coupling due to autoionization levels there would be a net red shift of the resonance peak asso-

ciated with state $|2\rangle$. In this example, $|q|\sim10$ produces a net blue shift with increasing intensity.

2. Gaussian wave solutions

The experimentally observed profiles are actually inhomogeneously broadened because of focusing. We assume for these calculations that the laser is given by a TEM$_{00}$ Gaussian profile. Hence, the transverse intensity distribution is

$$I(r)=2I_0 e^{-2r^2/W^2}, \quad (45)$$

where W is the laser waist. In this work, the Rayleigh range of the focal volume is of order 3.5 cm whereas the atomic beam diameter at the focal center is ≈0.64 cm, so to good approximation the inhomogeneously broadened MPI rate Γ' is given by

$$\Gamma'(\Delta)\propto2\pi\int_0^{\infty}dr\,r\Gamma(\Delta,I(r)). \quad (46)$$

Figure 16 shows calculations of this integral. It is assumed for these results that $\gamma_{12}=\sqrt{\gamma_{11}\gamma_{22}}$ and $\gamma_{11}=\gamma_{22}$. These model calculations illustrate that the inhomogeneously broadened resonance profile associated with state $|2\rangle$ remains narrow and "unshifted," with increasing intensity, while that of state $|1\rangle$ is significantly broadened and shifted to red. Interestingly, the power-law dependence of the state $|2\rangle$ peak heights, $\Gamma_{pk}^{(2)}\propto I^{1.6}$, is recovered when values of q, $\overline{\gamma}_{22}$, $\overline{\nu}_{22}$, and $\overline{\nu}_g$ are chosen so that the position of the state $|2\rangle$ resonance peak remains independent of intensity. However, the model calcula-
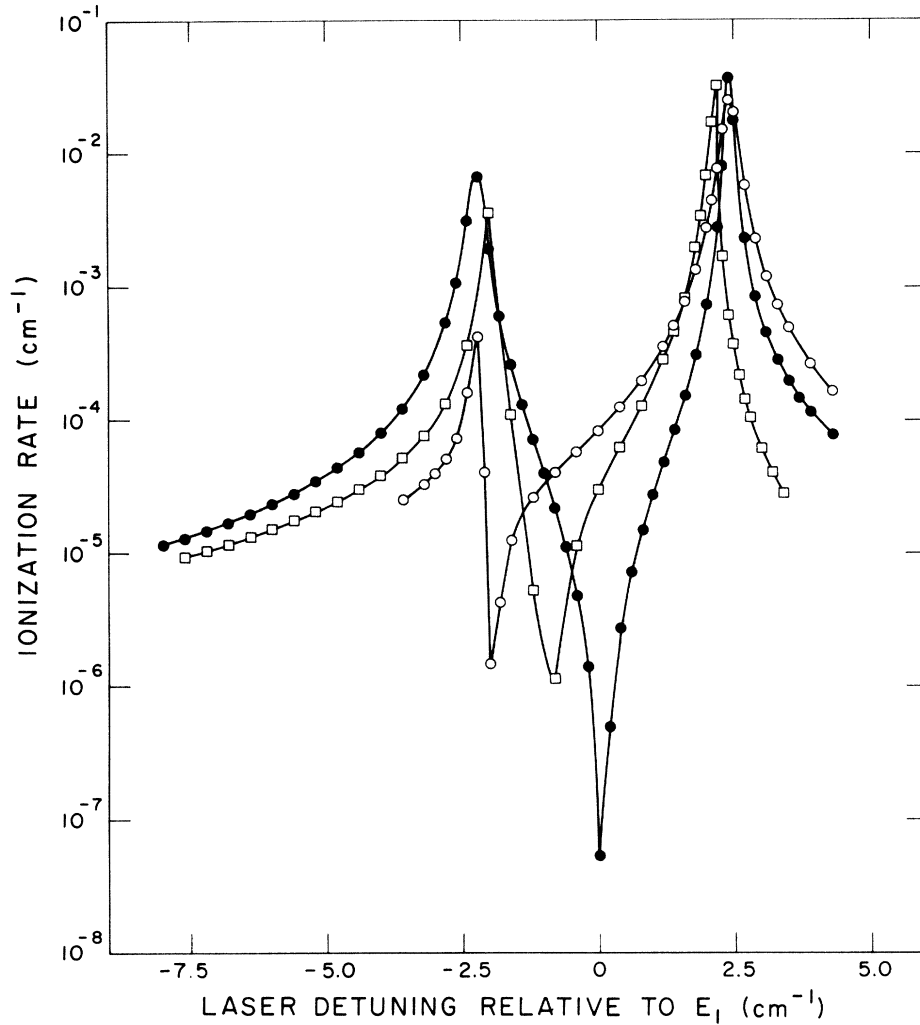
FIG. 14. Model calculations of MPI for circular polarization and a plane-wave light distribution: O, $q = +10.0$; □, $q = 0.0$; ●, $q = -10.0$. The other model parameters are fixed: $\bar{\Omega}_{2g} = 0.06$ cm^{-1}, $\Omega_{2g}/\Omega_{1g} = 3$, $\bar{\gamma}_{11} = \bar{\gamma}_{22} = 0.1$ cm^{-1}, $\bar{v}_g = 1.0$ cm^{-1}, $\bar{v}_{11} = -1.0$ cm^{-1}, and $\bar{v}_{22} = 0.70$ cm^{-1} with $I = 1$ GW/cm^2.

tions reproduce this behavior over a narrower range of intensities than was observed for the data. It is also notable that these model calculations do *not* reproduce the extended red wing behavior of the data for the resonance due to state $|1\rangle$. The cause of the extended wing features is traced in Sec. VI to temporal fluctuations ignored in this analysis. Chaotic fields produced by multimode pulse dye lasers exhibit large fluctuations in the field strength in contrast to the simplistic assumption of a uniform temporal pulse. Last, the near-resonant profile behavior was found to be relatively independent of combinations of γ_{12} and q such that

$$|\gamma_{12}q| \approx \text{const}.$$

This is shown in Fig. 16 for the case of the state $|1\rangle$ resonance but it also holds for state $|2\rangle$. A factor-of-5 reduction of γ_{11}, γ_{22}, and γ_{12} produce $\leq 50\%$ changes of the peak profile behavior.

C. Model profiles, linear polarization

Calculations of an inhomogeneously broadened, isolated resonance proceed similarly. The results of Fig. 17 were obtained by evaluating the integral of Eq. (46) using Eq. (23) for the rate of MPI and Eq. (45) for the intensity distribution. The results in Fig. 17 are based on values such that $\gamma_r > \gamma_L, \Omega^{(2)}, A$. The numerical results exhibited the following intensity scaling laws for the MPI linewidth $\gamma^{(2+1)}$, peak photoion yield $\Gamma_{pk}^{(2+1)}$, and total integrated photoion yield $S^{(2+1)}$:

$$\gamma^{(2+1)} \propto I^{1.00},$$

$$\Gamma_{pk}^{(2+1)} \propto I^{1.00},$$

$$S^{(2+1)} \propto I^{2.00}.$$

However, the model profiles always manifest a more extended blue wing in contrast to the data which show
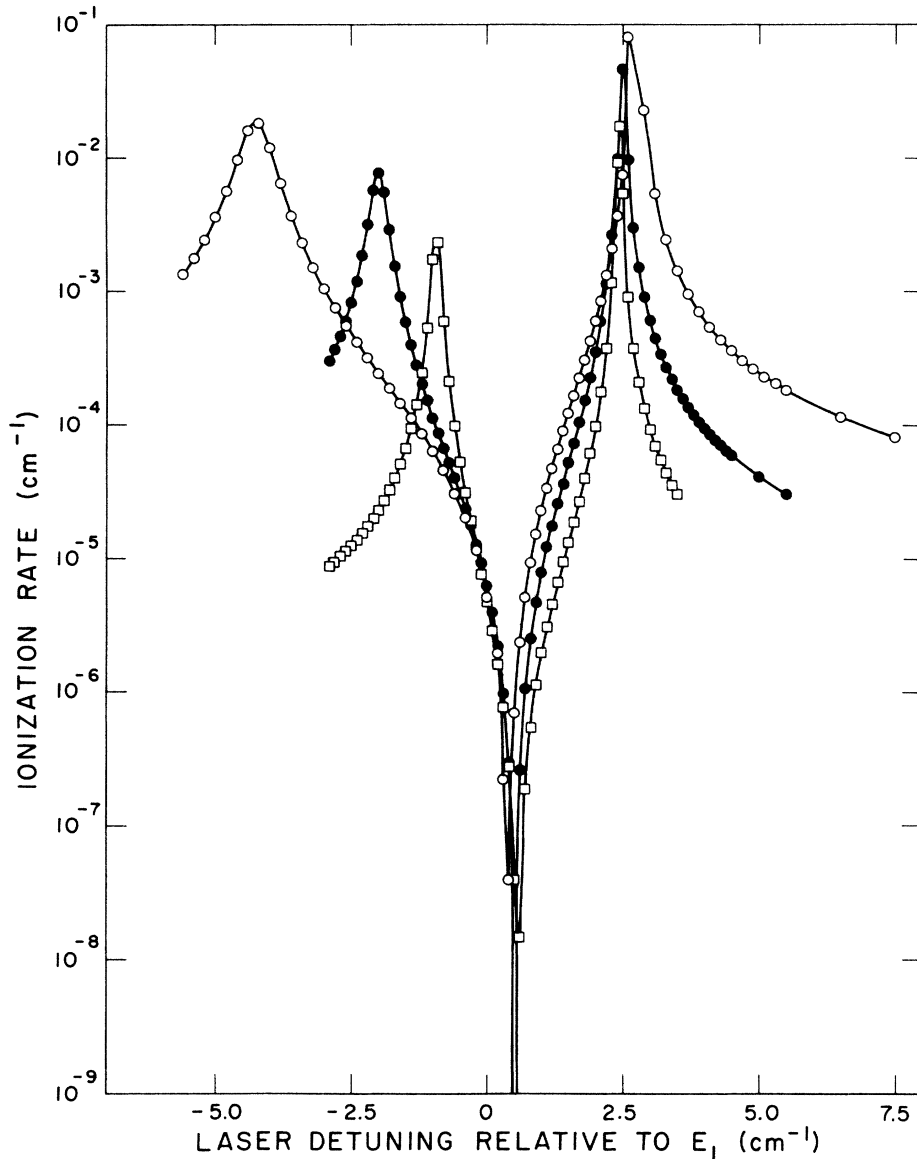
FIG. 15. Intensity dependence of model calculations assuming a plane-wave light distribution: $\square$, $I = 0.5$ GW/cm^2; $\bullet$, $I = 1.0$ GW/cm^2; $\circ$, $I = 2.0$ GW/cm^2. Other model parameters are fixed: $q = -12.0$, $\bar{\Omega}_{2g} = 0.06$ cm^{-1}, $\Omega_{2g}/\Omega_{1g} = 3$, $\bar{\gamma}_{11} = \bar{\gamma}_{22} = 0.1$ cm^1, $\bar{v}_g = 1.2$ cm^{-1}, $\bar{v}_{11} = -0.45$ cm^{-1}, and $\bar{v}_{22} = 0.85$ cm^{-1} when $I = 1$ GW/cm^2.

sharper onset of resonance near the field-free positions of the intermediate states. One can reduce this discrepancy by assuming smaller values for γ_r but then the scaling laws are no longer recovered; in the limit $\gamma_r^2 \ll \gamma_L^2$, $\Gamma_{pk}^{(2+1)} \propto I^{2.0}$. It is noted lastly that these model profiles are quite sensitive to variations of the photoionization rate γ_r as shown in Fig. 17(b).

VI. ANALYSIS AND DISCUSSION

A. Circular polarization

Calculations of inhomogeneous profiles show that the resonance associated with state $|2\rangle$ will generally remain narrow as a result of two effects. First, a quadratic shift of state $|2\rangle$ due to the $6pnd$ $J^\pi = 3^-$ levels nearly cancels a corresponding shift of the ground state, so the net separation of these two levels roughly equals the field-free separation. Second, the real part of the Raman scattering operator leads to a repulsion of the $6snd$ $J = 2$ doublet states. This effect is analogous to a second-order perturbation and leads to nonquadratic shift behavior of the doublet resonances.[10] The latter effect would also help account for the slight blue shift of state $|2\rangle$ observed in the intensity-dependent studies of the $n = 22$ doublet. Estimates of $\delta\omega_{22} - \delta\omega_g$ for this state indicate it should manifest an increasing red shift with increasing intensity in the absence of a Raman coupling.
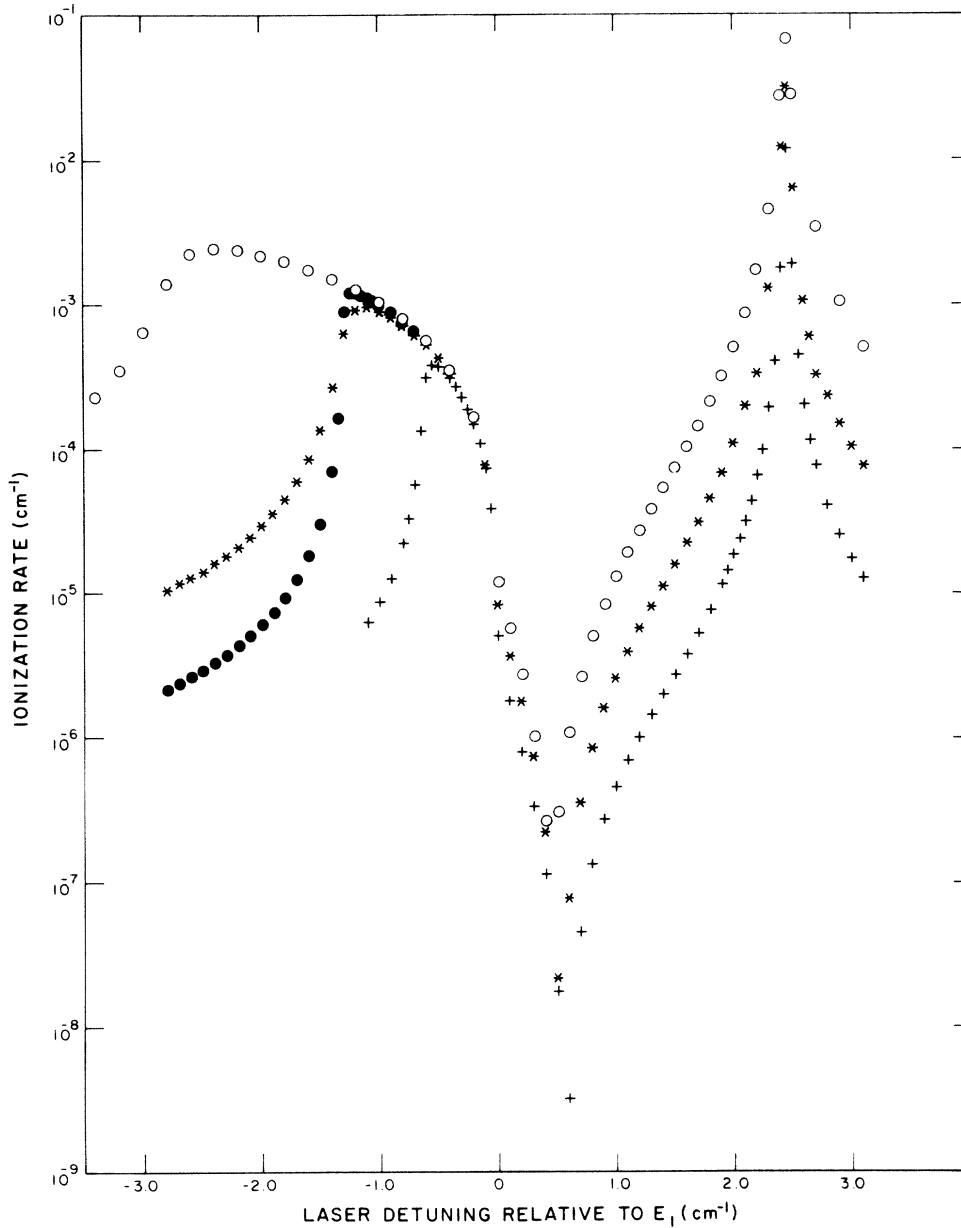
FIG. 16. Intensity dependence of model calculations assuming a Gaussian field distribution $I(r)=2I_0 e^{-2r^2}$ in Eq. (46): $+$, $I_0=0.5$ GW/cm^2; $*$, $I_0=1.0$ GW/cm^2; $\circ$, $I_0=2.0$ GW/cm^2. For these cases, $q=-12.0$, $\bar{\Omega}_{2g}=0.06$ cm^{-1}, $\Omega_{2g}/\Omega_{1g}=3$, $\bar{\gamma}_{11}=\bar{\gamma}_{22}=0.1$ cm^{-1}, $\bar{\nu}_g=1.2$ cm^{-1}, $\bar{\nu}_{11}=-0.45$ cm^{-1}, $\bar{\nu}_{22}=0.85$ cm^{-1} when $I_0=1$ GW/cm^2. Model calculations are shown ($\bullet$) when $\bar{\gamma}_{11}=\bar{\gamma}_{22}\to 0.02$ cm^{-1}, $q\to -60.0$, and $I_0=1.0$ GW/cm^2, and other parameters as before.

Calculations for the quadratic shifts of the excited states show the magnitude and sign of $\delta\omega_{11}$ and $\delta\omega_{22}$ are dependent on the value of the singlet-triplet mixing coefficient β of the $6snd$ $J=2$ doublets. This mixing coefficient is strongly altered by CI in the vicinity of the $5d\,7d$ $^1P_2$ perturber. Previous assignments of β (Ref. 26) cause $\delta\omega_{22}$ to change sign with respect to the asymptotic values when $26 \leq n \leq 34$ while $\delta\omega_{11}$ changes sign only for

$n=26$. By contrast, values of β based on fits of the relative absorption oscillation strengths $f(6s\,6p\,^1P_1^\circ \to 6snd$ $J=2)$ lead to a sign switch of the quadratic shifts at $n=27$. The latter is indeed borne out by the experimental data of Figs. 5b and 6b which show that the resonance profiles of the $n=27$ doublet switch characteristics in contrast to the behavior of the other doublets. Measurements of the peak shifts of $|2\rangle$ also bear this out, as
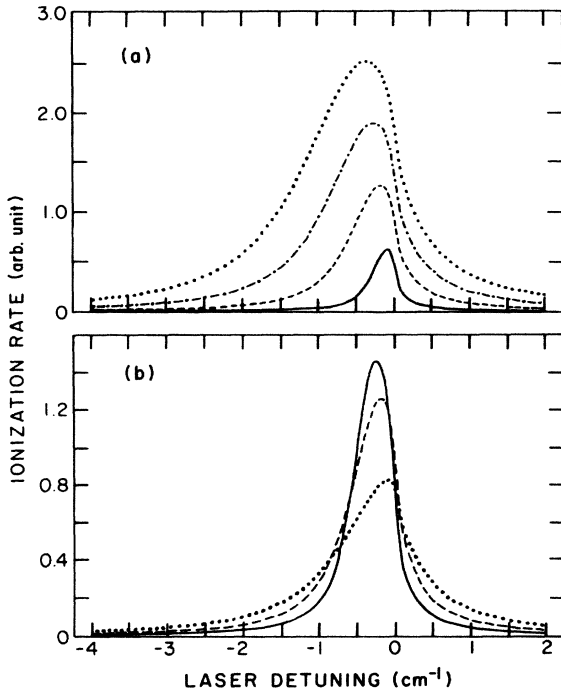
FIG. 17. Model calculations for the case of linear polarization using the rate-equation formulation of Eq. (23) and Gaussian field distribution $I(r) = 2I_0 e^{-2r^2}$ in Eq. (46). (a) shows the intensity-dependent behavior: ———, $I_0 = 0.5$ GW/cm^2; — — —, $I_0 = 1.0$ GW/cm^2; —·—·—·, $I_0 = 1.5$ GW/cm^2; ···, $I_0 = 2.0$ GW/cm^2. Other parameters are $S = 0.5$ cm^{-1}, $\gamma_L = 0.2$ cm^{-1}, $\Omega = 0.2$ cm^{-1}, $\gamma_r = 1.0$ cm^{-1} when $I_0 = 1.0$ GW/cm^2. (b) shows similar model calculations for various photoionization rates γ_r: ———, $\gamma_r = 0.5$ cm^{-1}; — — —, $\gamma_r = 1.0$ cm^{-1}; ···, $\gamma_r = 2.0$ cm^{-1} when $I_0 = 1$ GW/cm^2. The parameters S, γ_L, and Ω are the same as (a).

shown in Fig. 18.

Quantitative comparison of the measured shifts with calculations is not attempted in this work since bandwidth, saturation, and inhomogeneous line-broadening effects must be treated accurately. Field fluctuations of a chaotic light field are expected to enhance field-induced shifts and widths, by as much as a factor of 3,[32] but saturation effects generally diminish this.[32] Finally, inhomogenous broadening effects tend to produce smaller observed shifts since a more extended volume of lower intensity dominates in the formation of the profiles. Clearly, the assumptions of a single-frequency, TEM$_{00}$ Gaussian distribution and square temporal pulse of light intensity are too simplistic. Nevertheless, the relative behavior of the resonance shifts suggests greater validity for our trend of $d\beta/d\nu$ since none of the mentioned effects change the signs of the light shifts. The relative magnitudes of the shifts may vary due to saturation effects since this depends on the ratio Ω/A of the bound-bound Rabi rate Ω and radiative decay rate A;[32] however, the intensities were such that $\Omega/A \geq 10$ for all levels, so saturation effects are expected to remain constant for the spectra shown.
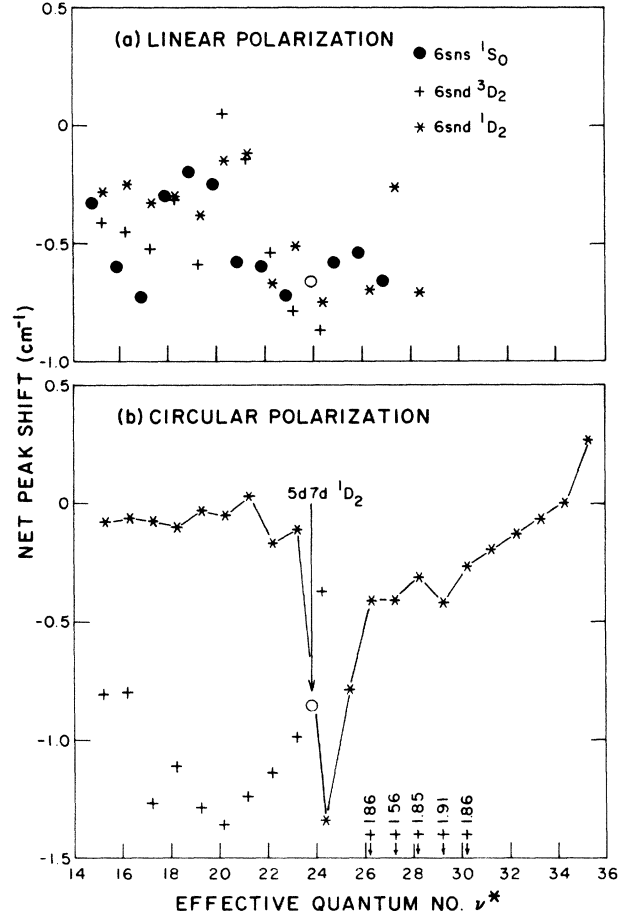

FIG. 18. Net shift of the resonant MPI peak positions when $I_0 \sim 1.1$ GW/cm^2. These data are based on spectra obtained with the CEM detector and bias fields <0.2 V/cm. The net shifts are calculated relative to the level positions of Ref. 12: (a) linear polarization, (b) circular polarization. The line connecting the $^1D_2$ data is drawn to aid visual continuity.

A somewhat surprising result of the model calculations for circular polarization is the independence of the near-resonant shapes of the MPI profiles with γ_{11}, γ_{22} when $q < -10$ and $\gamma_{12}q \sim$ const. The results of model calculations imply sizable changes of ionization rates do not result in commensurate changes of the peak profile behavior. The magnitudes of γ_{11}, γ_{22}, and γ_{12} depend on the product of final-state density a_ε^2 and the Rydberg electron overlap $O(n,\nu_\varepsilon)$. The former is relatively constant but the overlap function varies sharply with n, so calculated values of γ_{11}, γ_{22}, and γ_{12} range from 0.0001—0.01 cm^{-1} for $n \geq 18$. The data do not show evident variation of the near-resonant profiles due to state $|2\rangle$ throughout the spectrum (except $n = 27$ where $\delta\omega_{11} > 0$ and $\delta\omega_{22} < 0$). This even holds for cases where the calculated values of γ_{11}, γ_{22}, and γ_{12} increase an order of magnitude when $3\hbar\omega_L < \varepsilon(6p_{1/2})$, i.e., $n < 18$. These MPI profiles behave quite similarly to those with $n \geq 18$. The data for $n = 16$

are shown in Fig. 19 for comparison.

In contrast, the profile behavior associated with state $|1\rangle$ resonances alters near the $5d\,7d\,^1D_2$ perturber. In particular, the $n=26$ resonance has a much more distinct minimum. This is consistent with the model calculations shown in Fig. 14 which indicate the interference node is pushed nearer state $|1\rangle$ for $q>0$.

B. Linear polarization

The data do not show evident interference and coupling effects between $|1\rangle$ and $|2\rangle$. The data can be fit by adding, incoherently, two scaled profiles of an isolated peak. It is presumed, thus, that the excited-state quadratic shifts and $\delta\omega_{12}\approx 0$ and any coupling γ_{12} of the doublet states due to continuum states cancels when summing over the two channels of photoionization, so that Eq. (22) reduces to

$$\Gamma_T^{\text{lin}} \propto \gamma^{\text{lin}}(\,|a_1|^2 + |a_2|^2\,) .$$

It is notable in this regard that peak positions of all resonances manifest nearly the same red shift as shown in Fig. 18. (A slight increase for $n \gtrsim 30$ is most probably an artifact of not sufficiently resolving the doublet states.) It is also inferred (based on results of model calculations) that

$$\sigma_{11}(n) \approx \sigma_{22}(n) \approx \sigma_{22}(n')$$

since there is little apparent variation of the profile asymmetries with n, l, or S. The same, red asymmetry was observed for all resonances which suggests its origin is due to a common feature of the MPI process, the ac Stark
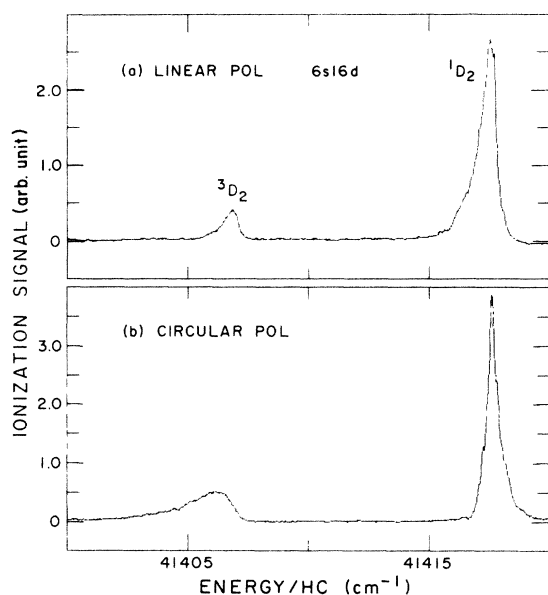
shift of the ground state. Assuming both are true, the integrated yield of each profile should provide a relative measure of the two-photon Rabi rate to populate the intermediate states. Such data are presented in Fig. 20 where the total integrated yield of each doublet is plotted relative to its effective quantum number of ν_n. The asymptotic trend for n far from the perturber follows the expected Rydberg scaling law ν^{-3} for $f(6s\,6p\,^1P_1^\circ \rightarrow 6snd$ $J=2)$ values.

Near the perturbing level, these data manifest a dispersion-type profile quite characteristic of CI effects. The effect of CI will mix the $6snd$ $J=2$ channels with the $5dnd$ $J=2$ channels. Approximating for the case of just two channels, the wave functions mix as

$$|6snd\ J=2'\rangle' = \cos\delta\,|6snd\rangle - \sin\delta\,|5dn'd\rangle ,$$

$$|5dn'd\ J=2\rangle' = \sin\delta\,|6snd\rangle + \cos\delta\,|5dn'd\rangle .$$

Multichannel-quantum-defect-theory analysis treats the addition of a perturber state as an accumulation of phase and shows that observables such as $\delta(\nu_n)$ vary smoothly like a dispersion function from $0 \rightarrow \pi$ for ν_n "around" the perturber.[33] [Previous analysis has shown that $|\gamma(\nu)|^2 \propto |\sin\delta(\nu)|^2$ is given by a Lorentzian-like distribution centered at the $5d\,7d\,^1D_2$ perturber.][24,34]

The two-photon Rabi rate is actually a coherent superposition of virtual transitions through all intermediate $J^\pi = 1^-$ states so interference is expected due to virtual transitions through the $5d\,6p$ $J^\pi = 1^-$ levels. The magnitude of interference will be large if

$$f(5d\,6p\ J^\pi = 1^- - 5d\,7d\,^1D_2) \sim 0.1$$

so that

$$f(^1S_0 - 6s\,6p\,^1P_1^\circ)f(6s\,6p\,^1P_1^\circ - 6snd\,^1D_2)$$

$$\approx f(^1S_0 - 5d\,6p\ J^\pi = 1^-)f(5d\,6p\ J^\pi = 1^- - 5d\,7d\,^1D_2) .$$

The dispersion behavior in Fig. 20 is considered to be the result of the variation of $\delta(\nu_n)$; admixture of $5d\,7d\,^1D_2$

FIG. 19. MPI spectra due to the $6s\,16d$ $J=2$ intermediate resonances: (a) linear polarization, (b) circular polarization. These data were obtained with the CEM detector and $I_0 \sim 1$ GW/cm^2. The two-photon energy scales are significant only in a relative sense (± 0.1 cm^{-1}).
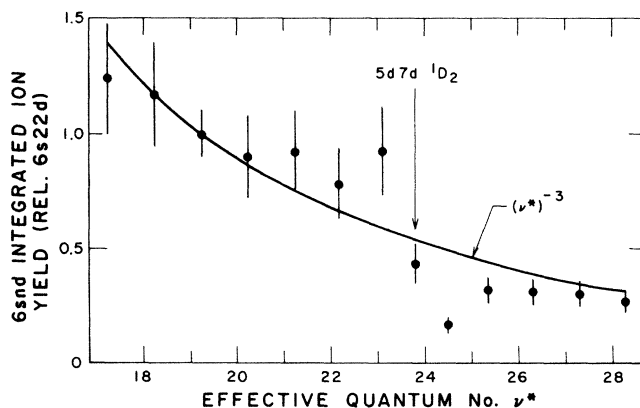

FIG. 20. MPI integrated ion yield (linear polarization) vs effective quantum number ν^*. These data represent the total integrated ion yield of each $6snd$ $J=2$ doublet relative to the $n=22$ data.

will coherently add in the numerator of Eq. (14) on one side of the perturbing state while destructively adding on the other. A quantitative fit of the data requires more detailed knowledge of $f(6s^2\,{}^1S_0 - 5d\,6p\quad J^\pi = 1^-)$ and $f(5d\,6p\;J^\pi = 1^- - 6snd\;J = 2)$ values.

This brings up an interesting point concerning assignments of γ and β. Previous analyses of γ based on lifetime[24] and level position data[34] have shown that $|\gamma(\nu_n)|^2$ is given by a Lorentzian-like distribution centered at the perturbing state; however, analyses of β based on hfs measurements find $\beta(\nu_n)$ follows a dispersive function centered near $n = 26$, i.e., $d\beta/d\nu \sim$ max at $n = 26$.[25,26] No explanation for this apparent "discrepancy" has been given. By contrast, results of this work suggest both γ and β are given by distributions centered at the perturber position. The latter result seems more intuitively correct.

C. Bandwidth effects

The intensity-dependent behavior of the data obtained with linear polarization was reproduced with the assumption $\gamma_r^2 \gg \gamma_L^2$. However, order-of-magnitude calculations yielded values $\gamma_r \sim \Omega^{(2)} \sim 0.05$ cm^{-1}/GW cm^2 which are clearly smaller than the time-averaged bandwidth $\bar{b}$ of the laser and the zero-intensity linewidth limit $\gamma_L^0 \approx 0.2$ cm$^{-1} \approx 2\bar{b}$. The apparent contradiction can be resolved by noting that the laser field actually consists of several modes designated i, with mode bandwidth $b_i < 0.01$ cm^{-1}.

Studies of resonant MPI in atomic hydrogen (using linear polarized light) have shown that averages of the rate description of Eq. (23) for a multimode laser are consistent with our observed scaling laws when the photoionization rate is larger than the *mode* bandwidth.[35] More generally, Ref. 35(b) showed $\Gamma_{pk} \propto \Omega$ when $\gamma_r^2 \gg (2b_i)^2$ and $\Gamma_{pk} \propto \Omega^2$ when $\gamma_r^2 \ll (2b_i)^2$. In these studies, the laser electric field is modeled as a superposition of modes,

$$E(t) = \varepsilon(t)\exp(-i\omega_0 t) + \text{c.c.} ,$$

$$\varepsilon(t) = \sum_i \varepsilon_i \exp(-t^2/\tau^2)\exp(-i\,\Delta\omega_i t + \phi_i) ,$$

where ε_i are the amplitudes of each mode, $\Delta\omega_i$ is the longitudinal frequency spacing from ω_0, ϕ_i the (random) phase of each mode, and τ the envelope duration of the pulse. The values of ϕ_i were chosen to fit the calculated mode beating to temporal fluctuations of $I(t)$ very similar in nature to those observed in our study [see Fig. 2.12 of Ref. 35(b)]. The data of Ref. 35 are consistent with chaotic field models which show that averages of the ionization rate of Eq. (1) over temporal fluctuations recover the extended wing behavior of the MPI profiles. The wing behavior is a consequence of stochastic fluctuations of $E(t)$ which can be several times larger than the mean value for a single mode pulse. This effect is a homogeneous line-broadening process since all atoms see the same temporal fluctuations, so it will cause greater enhancement of the shifted wing than effects of spatial averaging.

Thus, knowing the structure of ϕ_i of the laser, the data obtained with linearly polarized light could be reduced to give absolute values of the bound-bound Rabi rate Ω and photoionization rate γ_r. This will be left for later

analysis. It is noted, though, that the intensity-dependent behavior for both polarizations implies $\gamma_r^2 \gtrsim 2b_i$, even at the lowest intensities studied, which implies a lower bound value for $\sigma_{ii}(n) \gtrsim 5 \times 10^{-18}$ cm^2, $16 \leq n < 40$. This is larger but not grossly inconsistent with values given by Eq. (42).

VII. CONCLUSION

Two-photon resonant, three-photon ionization spectra of Ba have been measured for linear and circular polarization. Interference and coupling of the $J = 2$ states of each $6snd$ doublet occurred when circularly polarized light is used for excitation. This behavior has been treated with an effective Hamiltonian which shows that the interference node and resonance peaks are affected by a Raman coupling which results primarily from the $6pnd\;J = 3$ autoionization levels. In the case of the $6snd\;J = 2$ states of Ba the real part of the Raman coupling $\delta\omega_{12}$ is sufficiently large that it produces nonquadratic light shift behavior. The other notable feature of this model is that its effective matrix elements depend on the singlet-triplet mixing coefficient β in a manner which qualitatively matches the data. However, values of β based on these model calculations (and fits of photoabsorption data) differ with previous assignments[25,26] for principal quantum numbers n near the perturber. The cause of the disagreement is not fully understood yet, but it suggests new efforts be made to clarify the assignments. Toward this end, accurate relative measurements of the oscillator strengths $f(6s\,6p\,{}^1P_1^\circ - 6snd\;J = 2)$ could provide a sensitive probe of β.

Channel interference and Raman coupling effects were not evident in the spectra obtained with linear polarization. Instead, all resonance profiles exhibited the same asymmetric broadening to the red which is traced to the ground-state quadratic shift. It is speculated that this behavior results because the additional channel of photoionization to $J^\pi = 1^-$ levels leads to cancellation of the cross terms $\gamma_{12}a_1^*a_2$, $\delta\omega_{12}$, and the excited-state quadratic shifts. Quantitative analysis of this speculation awaits additional knowledge of the $6pnl\;J^\pi = 1^-$ level structure.

Measurements of MPI using linear polarization provide a simpler means of measuring the bound-bound Rabi rate Ω and the excited-state photoionization rates γ_{ii} since in the absence of significant interferences these data can be treated with an isolated rate formulation. An interesting, preliminary result of this work is the observation that Ω may provide a complementary measurement of the perturber admixture γ and its phase in addition to lifetime data that only measure $|\gamma|$. [In this regard, measurements of the oscillator strengths $f(5d\,6p\;J^\pi = 1^- - 5d\,7d\,{}^1D_2)$ would also be useful.]

Bandwidth and saturation effects have not been treated explicitly in this work but these may become an interesting outcome of the work. The $J = 2$ Rydberg series and $5d\,7d\,{}^1D_2$ perturber state provide a set of coupled levels where the ratio of the bound-bound Rabi rate and radiative decay Ω/A "slew" in a smooth way. One could use this to turn saturation effects on and off. In this work the

intensities were such that $\Omega/A > 10$ for all levels, so saturation effects are expected to remain constant.[32] It would be very interesting, though, to compare the effective linewidths and profiles of this experiment, which represents a chaotic light field limit, to those obtained with a single mode source.

ACKNOWLEDGMENTS

*Present address: Joint Institute for Laboratory Astrophysics, National Bureau of Standards and University of Colorado, P.O. Box 440, Boulder, CO 80309-0440.

[1]H. H. Bebb, Phys. Rev. 149, 25 (1966).

[2]C. E. Theodosiou, L. Armstrong, M. Crance, and S. Feneuville, Phys. Rev. A 19, 766 (1979), and references therein.

[3]M. Crance, J. Phys. B 11, 1931 (1978); G. Petite, J. Morellec, and D. Normand, J. Phys. (Paris) 40, 115 (1979).

[4]J. H. Eberly, Phys. Rev. Lett. 42, 1049 (1979).

[5]A. T. Georges and P. Lambropoulos, Phys. Rev. A 15, 727 (1977).

[6]P. L. Knight, Opt. Commun. 31, 148 (1979).

[7]B. Ritchie, Phys. Rev. A 21, 629 (1980).

[8]S. N. Dixit, P. Lambropoulos, and P. Zoller, Phys. Rev. A 24, 318 (1981).

[9]G. Leuchs, G. Alber, and S. J. Smith, in Laser Spectroscopy VII, edited by T. W. Hänsch and Y. R. Shen (Springer-Verlag, Berlin, 1985), p. 216.

[10]J. Reif, M. Poirier, J. Morellec, and D. Normand, J. Phys. B 17, 4151 (1984).

[11](a) Level positions and f values of the $6p_{3/2}nd$ $J^\pi = 3^-$ states are based on results from N. H. Tran, P. Pillet, R. Kachru, and T. F. Gallagher, Phys. Rev. A 29, 2640 (1984). (b) Level positions and relative f values of the $6p_{1/2}nd$ and $6p_{3/2}nd$ $J^\pi = 3^-$ states are from R. Kachru, H. B. van Linden van den Heuvell, and T. F. Gallagher, Phys. Rev. A 31, 700 (1985), and references therein.

[12]M. Aymar, P. Camus, M. Dieulin, and C. Morillon, Phys. Rev. A 18, 2173 (1978).

[13]B. M. Miles and W. L. Wiese, At. Data 1, 1 (1969).

[14]M. G. Littman, Opt. Lett. 3, 138 (1978); R. Mahon and F. S. Tomkins, IEEE J. Quantum Electron. QE-18, 913 (1982).

[15]B. A. Palmer, R. A. Keller, and R. Engleman, Jr., An Atlas of Uranium Emission Intensities in a Hollow Cathode Discharge (Los Alamos Scientific Laboratory Report No. LA-8251-MS) (National Technical Information Service, Springfield, VA, 1980).

[16]M. Pellin (private communication).

[17]E. Hinnof and W. Ohlendorf, J. Chem. Phys. 50, 3005 (1969).

[18]W. R. S. Garton and F. S. Tomkins, Astrophys. J. 158, 1219 (1969).

[19]The upper bound value for the residual field is based on measurements of the largest thermionic emission current that flowed between the plates and values of the resistors used to isolate the collection and/or guard plates from ground.

[20]J. A. Armstrong, J. J. Wynne, and P. Esherick, J. Opt. Soc. Am. 69, 211 (1979).

[21]The appearance of the $6snp$ series with elliptically polarized light could also have been an artifact of second-harmonic generation (SHG) that can occur when rotating the optic axis of the crystalline quartz plates of the compensator. Filtering possible SHG, uv radiation with a glass window precluded any such complication.

[22]T. F. Gallagher, W. Sandner, and K. A. Safinya, Phys. Rev. A 23, 2969 (1981).

[23]J. H. Shirley, Phys. Rev. 138, B979 (1965).

[24]M. Aymar, R. J. Champeau, C. Delsart, and J. C. Keller, J. Phys. B 14, 4489 (1981).

[25]H. Rinneberg and J. Neukammer, Phys. Rev. A 27, 1779 (1983).

[26]E. R. Eliel and W. Hogervorst, J. Phys. B 16, 1881 (1983).

[27]R. D. Cowan, The Theory of Atomic Structure and Spectra (University of California Press, Berkeley, 1981), Sec. 11-7.

[28]R. J. Fonck, F. L. Roesler, D. H. Tracy, K. T. Lu, F. S. Tomkins, and W. R. S. Garton, Phys. Rev. Lett. 39, 1513 (1977), and unpublished data therein from F. S. Tomkins (private communication).

[29]U. Fano and J. W. Cooper, Rev. Mod. Phys. 40, 441 (1968).

[30]S. A. Bhatti and W. E. Cooke, Phys. Rev. A 28, 756 (1983).

[31]Reference 26, Sec. 18.7.

[32]G. H. Alber and P. Zoller, J. Phys. B 13, 4567 (1980).

[33]See Refs. 24, 25, and 27, and references therein.

[34]M. Aymar and O. Robaux, J. Phys. B 12, 531 (1979).

[35](a) D. E. Kelleher, M. Ligare, and L. R. Brewer, Phys. Rev. A 31, 2747 (1985); (b) L. R. Brewer, Ph.D. thesis, Massachusetts Institute of Technology, 1984.